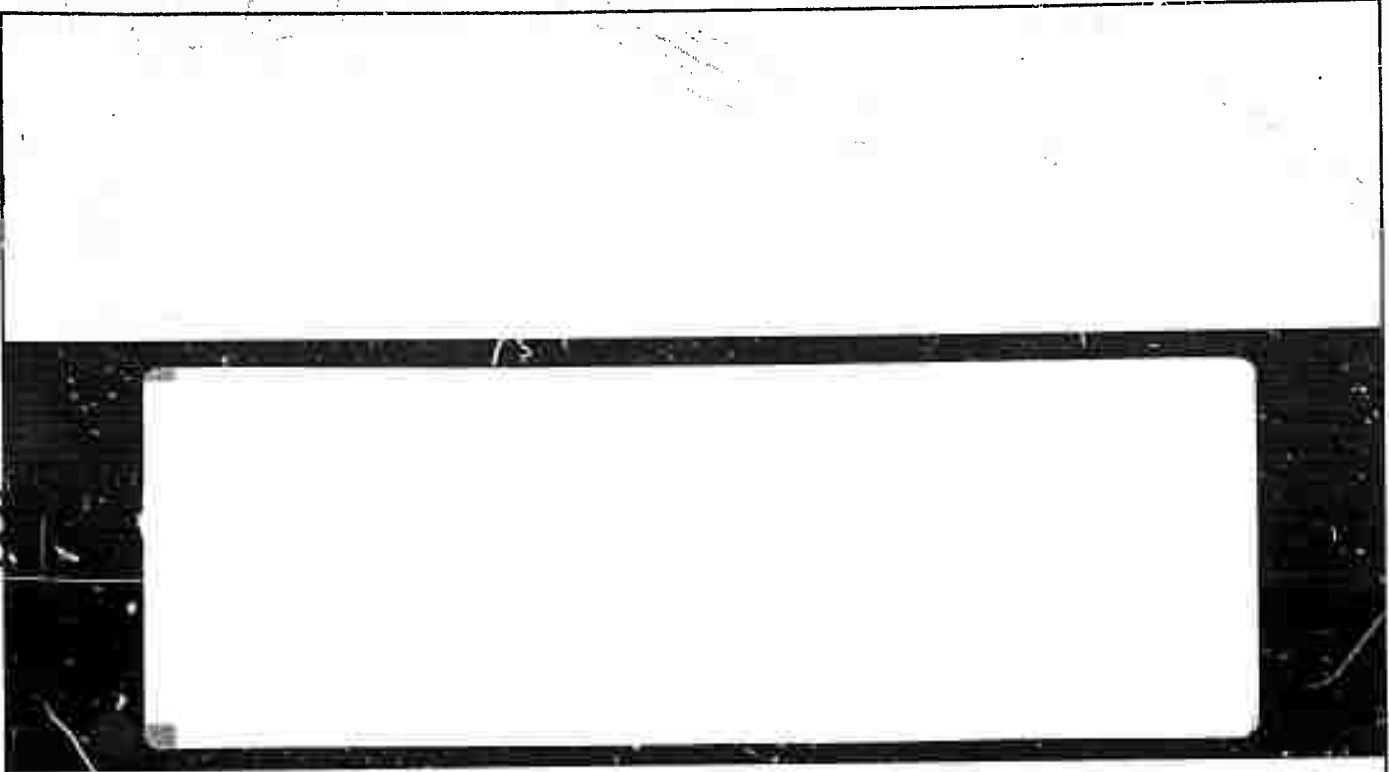


6000-9209.4.0

THE BOEING COMPANY

SCIENTIFIC RESEARCH LABORATORIES

AD 740216



D D C
REF ID:
APR 20 1972
RELEASER
B

Approved for public release; distribution unlimited. The findings in this report are not to be construed as an official Department of the Army position, unless so designated by other authorized documents.

THE **BOEING** COMPANY

AEROSPACE GROUP / SEATTLE, WASHINGTON

**BEST
AVAILABLE COPY**

Unclassified

Security Classification

DOCUMENT CONTROL DATA - R & D

(Security classification of title, body of abstract and indexing annotation must be entered when the overall report is classified)

1. ORIGINATING ACTIVITY (Corporate author)

The Boeing Company-Aerospace Group

2a. REPORT SECURITY CLASSIFICATION

Unclassified

3a. GROUP

NA

3. REPORT TITLE

A New Technique to Determine Amorphous Structure Using X-Ray Absorption Fine Structure

4. DESCRIPTIVE NOTES (Type of report and inclusive dates)

Final Report: Technical Report

5. AUTHOR(S) (First name, middle initial, last name)

Dale E. Sayers

6. REPORT DATE

1972

7a. TOTAL NO. OF PAGES

111

7b. NO. OF REFS

8a. CONTRACT OR GRANT NO.

DAHCO4 71 C 0010

9a. ORIGINATOR'S REPORT NUMBER(S)

b. PROJECT NO.

NA

c.

9b. OTHER REPORT NO(S) (Any other numbers that may be assigned this report)

d.

9209.4-P

10. DISTRIBUTION STATEMENT

Approved for public release; distribution unlimited.

11. SUPPLEMENTARY NOTES

12. SPONSORING MILITARY ACTIVITY

U. S. Army Research Office-Durham
Box CM, Duke Station
Durham, North Carolina 27706

13. ABSTRACT

A new theory for extended x-ray absorption fine structure (EXAFS) is presented which treats EXAFS as arising from the scattering of the ejected photoelectron by atoms surrounding the absorbing atom. The surrounding atoms are treated as a system of weak point scatterers which allows the scattered waves to be calculated using standard scattering theory. These scattered waves are included in the wave function of the ejected photoelectron and this is used to calculate the dipole transition matrix element from the x-ray absorption, which gives rise to oscillations in the absorption coefficient which depends on the positions of the surrounding atoms. The final result includes scattering factor, range and temperature terms and is general enough to handle any symmetry of atoms about the absorbing atom and any polarization state of the x-rays.

14. KEY WORDS

x-ray absorption spectra
copper
iron
germanium

germanium selenide
germanium oxides

**RESEARCH AND ENGINEERING DIVISION
BOEING SCIENTIFIC RESEARCH LABORATORIES**
P.O. Box 3999
SEATTLE, WASHINGTON 98124

D180 - 14436 - 1

**A New Technique to Determine Amorphous Structure
Using X-Ray Absorption Fine Structure**

Dale E. Sayers

D D C
RECORDED
APR 20 1972
REGISTRED
B

THE **BOEING** COMPANY

AEROSPACE GROUP / SEATTLE, WASHINGTON

SPECIAL TECHNICAL REPORT
THE STRUCTURE OF NON-CRYSTALLINE MATERIALS

Approved for public release; distribution unlimited

D180-14436-1

A NEW TECHNIQUE TO DETERMINE AMORPHOUS STRUCTURE
USING X-RAY ABSORPTION FINE STRUCTURE

BY

DALE E. SAYERS

Contract DAHC04 71 C 0010
Program Element Code: 61101D
ARPA Order No. 1562

Farrel W. Lytle, Principal Investigator
(206) 655-5574

The Boeing Company, Seattle, Washington 98124

Effective Date: February 4, 1971
Expiration Date: March 3, 1972

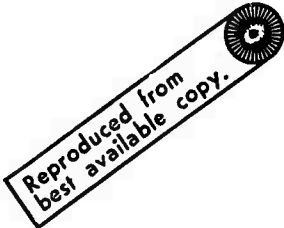
Amount: \$65,000

Disclaimer

The views and conclusions contained in this document are those of the authors and should not be interpreted as necessarily representing the official policies, either expressed or implied, of the Advanced Research Projects Agency or the U. S. Government.

Table of Contents

	Page
List of Tables	iii
List of Figures	iv
Abstract	vi
Chapter 1 Introduction	1
Chapter 2 Point Scattering; Theory of X-ray K Absorption Fine Structure	7
Chapter 3 A New Method for Structure Analysis Using the Fourier Transform of EXAFS	45
Chapter 4 Experimental Methods	58
Chapter 5 Application of EXAFS Technique to Structure Determination of Amorphous Ge, GeO ₂ and GeSe	66
A - Germanium	66
B - GeO ₂	76
C - GeSe	83
Chapter 6 Discussion and Conclusions	90
Appendix A Filtering Methods	96
Appendix B Atomic Structures for EXAFS	100
Appendix C Computer Program Listings	103
A - EXAFS Atomic Structure Program	103
B - Theoretical EXAFS Program	106
References	109



List of Tables

	<u>Page</u>
Table I	
Data for Back-Scattering in O, Ge and Se	23
Table II	
Input Data to Calculate EXAFS in Cu, Fe, and Ge	39
Table III	
EXAFS Structural Data for GeO ₂ , GeSe, SeGe	81

List of Figures

	<u>Page</u>
Figure 1 Examples of EXAFS for the Ge K edge in amorphous GeO ₂ and the Ge and Se K edges in GeSe.	2
Figure 2 Comparison of the factor kf(k) using (a) the free electron, (b) the screened coulomb, and (c) the Doyle and Turner scattering factors.	25
Figure 3 Comparison of the WKB phase shift using the Herman-Skillman potential and the fitted linear phase shift for Ge.	37
Figure 4 Comparison of theoretical and experimental EXAFS for copper and iron.	40
Figure 5 Comparison of theoretical and experimental EXAFS for germanium.	41
Figure 6 (a) Theoretical EXAFS for iron without the temper- ature and range terms, (b) temperature correction has been applied to curve (a), (c) the exponential attenuation has been applied yielding the theoretical curve in Fig. 4b.	42
Figure 7 Termination effects on the radial structure function of the theoretical Ge EXAFS of Fig. 5c. ($k_m = 15$).	53
Figure 8 (a) First shell Gaussian from the theoretical Ge rsf, (b) Calculated termination effect using eq.(3-15) for $k_m = 15$, (c) termination effects on (a) from direct integration with $k_m = 15$.	56
Figure 9 Diagram of the sample changing mechanism.	60
Figure 10 Schematic of the experimental apparatus.	61

	<u>Page</u>
Figure 11 Staggered and eclipsed linking of Ge tetrahedra.	68
Figure 12 Smoothed experimental EXAFS data for a) crystalline and b) amorphous Ge.	71
Figure 13 Radial structure functions of crystalline and amorphous Ge obtained from the curves of Fig. 11.	72
Figure 14 Plot of eq.(3-5) using the measured crystalline Ge amplitudes.	74
Figure 15 Comparison of crystalline and amorphous GeO_2 EXAFS.	77
Figure 16 Radial structure functions for crystalline and amorphous GeO_2 .	79
Figure 17 Transform of GeO_2 -hex data showing termination ripple and structure near $r=0$.	80
Figure 18 Comparison of crystalline and amorphous GeSe EXAFS for both Ge and Se edges.	85
Figure 19 Radial structure functions for crystalline and amorphous GeSe with respect to a Ge atom (19 a) and an Se atom (19 b) at the origin.	86
Figure 20 Comparison of the rsf's about the Ge and Se atom in amorphous GeSe.	88
Figure 21 Example of a frequency spectrum of the raw data using the fast Fourier transform.	98

Abstract

A new theory for extended x-ray absorption fine structure (EXAFS) is presented which treats EXAFS as arising from the scattering of the ejected photoelectron by atoms surrounding the absorbing atom. The surrounding atoms are treated as a system of weak point scatterers which allows the scattered waves to be calculated using standard scattering theory. These scattered waves are included in the wave function of the ejected photoelectron and this is used to calculate the dipole transition matrix element from the x-ray absorption, which gives rise to oscillations in the absorption coefficient which depends on the positions of the surrounding atoms. The final result includes scattering factor, range and temperature terms and is general enough to handle any symmetry of atoms about the absorbing atom and any polarization state of the x-rays. The result for unpolarized x-rays is used to calculate EXAFS for Cu, Fe and Ge, which are in excellent agreement with the observed spectra. Furthermore, the results of the theory can be used to show that when EXAFS is Fourier transformed it yields a radial structure function which determines the distribution of atoms about a particular kind of atom in the absorbing material. A method for determining amorphous structures is developed which compares the amorphous and crystalline radial structure functions and uses some of the parameters which are determinable from the crystalline data. It is shown that this technique has better resolution and can derive more information than the usual radial distribution analysis. Experimentally, a

fully automated apparatus is described which takes data with about .3% statistical counting error up to 2000 eV above the absorption edge. Data of this quality is necessary in order to obtain reliable structural information from EXAFS. The EXAFS technique was used to study the structure of amorphous Ge, GeO_2 , and GeSe. In Ge, the data was consistent with a continuous random network of Ge tetrahedra where the order decreases very rapidly beyond the second neighbor distance. The GeO_2 structure also appeared to be a tetrahedral network except that it was more ordered since the adjacent GeO_4 tetrahedra share the bridging oxygen atoms, thus giving a correlation between adjacent tetrahedra. In GeSe the power of the EXAFS technique to determine the structure about each kind of atom is demonstrated. The crystalline structure is a highly distorted NaCl structure with a 3:3 near neighbor coordination. The amorphous structure shows a splitting of the near neighbor peak indicating a tendency for both Ge and Se atoms to satisfy its ideal bonding requirements. The results of this work have allowed some basic conclusions to be drawn about the general nature of amorphous structures.

Chapter 1

Introduction

Extended x-ray absorption fine structure (EXAFS) refers to the oscillations in the x-ray absorption coefficient extending out to several hundred electron volts on the high energy side of an x-ray photoelectron edge. This phenomenon has been known for over 40 years since the first studies of Kronig¹. However, an adequate theory which quantitatively explains the observed spectra has not been proposed until now. Previous theories have been reviewed by Paratt² and more recently by Azaroff³. Fig. 1 shows examples of EXAFS for the Ge K edge in amorphous GeO_2 and for both the Ge and Se K edges in amorphous GeSe. Experimentally $\ln I_0/I = \mu x$ is plotted as a function of the ejected photoelectron energy where I and I_0 are the x-ray intensity with the absorber in and out of the beam, μ is the linear attenuation coefficient and x is the thickness of the absorber.

The first theory of EXAFS was proposed by Kronig¹ who suggested that the absorption anomalies (maxima and minima) were caused by Bragg reflection of the ejected photoelectrons from the planes in the crystalline lattice causing forbidden and allowed energies for the electron transition. A similar theory was proposed by Hayasi⁴ who felt that the Bragg reflected electrons led to oscillations in the dipole transition matrix element by setting up standing waves (quasi-stationary states) in the region around the absorption atom, thus increasing the overlap of the initial and final electron wave functions. Both

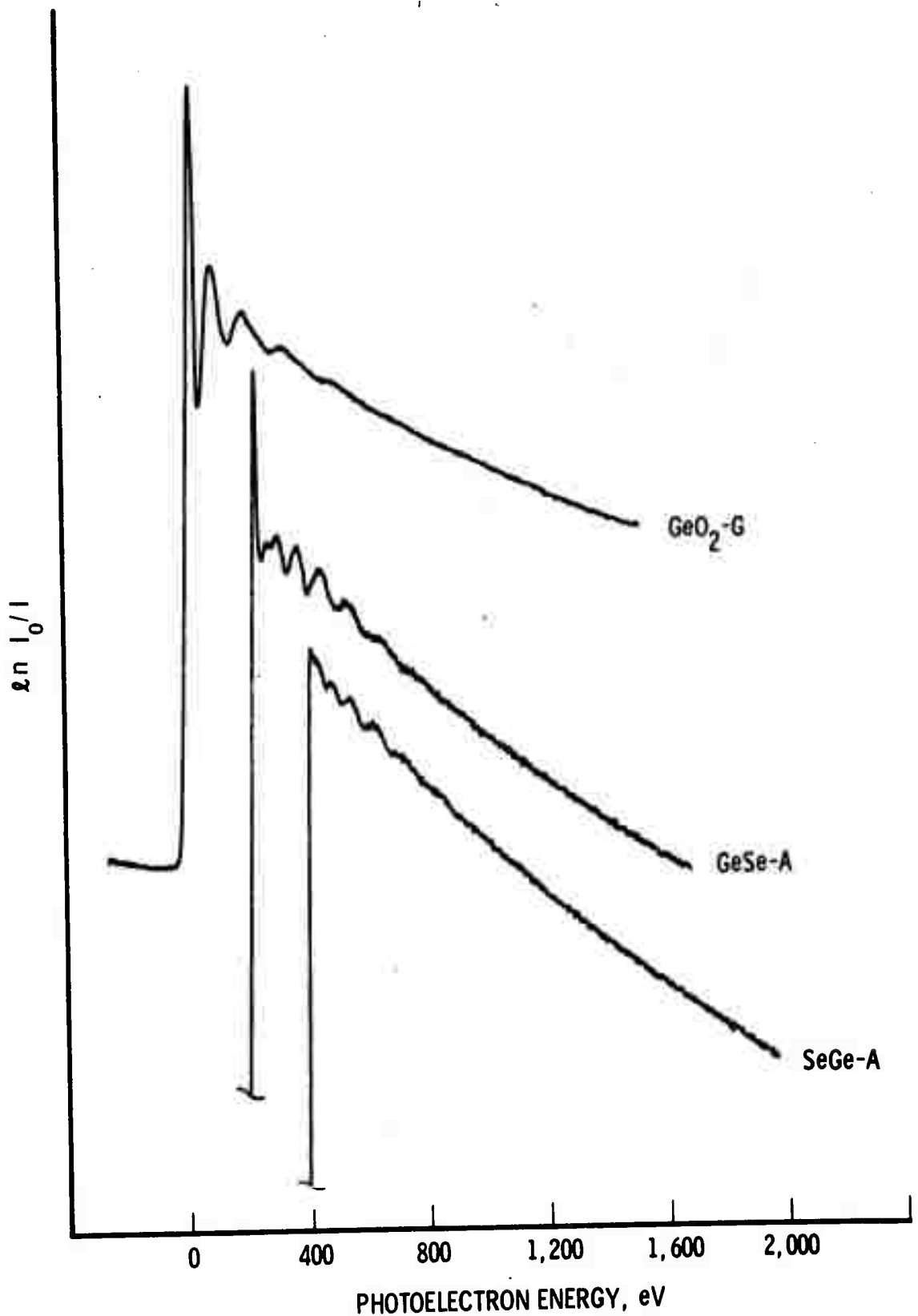


Figure 1

Examples of EXAFS for the Ge K edge in amorphous GeO_2 and the Ge and Se K edges in amorphous GeSe. The last two curves have been displaced downward and to the right for clarity.

various choices of scattering potentials. The final sro theory was proposed by Shiraiwa⁹, et al. who calculated scattering from individual atoms in a solid including multiple scattering from atoms, and included a range term for the photo-electron due mainly to inelastic scattering. They concluded that the single scattering dominated and arrived at a result which was similar to the other sro theories.

The results of all of the sro theories give expressions for the fine structure which are equivalent to

$$x \approx -\sum_j \frac{N_j}{r_j} \sin \left(2kr_j + 2\eta(k) \right) \quad (1-1)$$

where r_j is the distance from the absorbing atom to the j^{th} coordination shell, N_j is the number of atoms at r_j , k is the wave vector of the photoelectron and $\eta(k)$ is the phase shift of the photoelectron because of the potential of the absorbing atom. Most of the attempts to fit the data have involved finding the peak positions of the dominant shells, and the agreement with the data is typically within 5 - 10%. Some of the theories have added scattering factors⁵⁻⁹, temperature corrections⁸, and range terms⁹ to eq. (1-1), but attempts to calculate entire spectra which are in agreement with observed EXAFS have met with limited success. What is needed to calculate EXAFS which agree with experiment is a simple model which retains the physics of the problem but allows straightforward

calculation of the scattering using standard perturbation theory. A photoelectron range term, temperature correction, and the energy dependence of the scattering of the photoelectron must all be included in any quantitative result.

One of the difficulties in comparing theoretical and experimental results is that early experimental data was not of good resolution. The first experiments placed the absorber in the x-ray beam before the analyzing crystal and used film to record the spectra. The data collected in this way is usually of poor resolution and represents only the variations in the intensity through the absorber. It is difficult to divide by the unattenuated intensity so that $\ln I_0/I$ can be plotted. Another limitation of this technique is that EXAFS were recorded over only a few hundred eV above the edge, whereas EXAFS can be observed over 1000 eV above the edge. More recently EXAFS data has been collected using scintillation counters and a stepwise recording of the data. Most of the experiments have been manually operated so that the data recording is very tedious and is usually limited to only a few hundred eV above the edge, and the statistical counting error at each point is about 1%. In order to obtain EXAFS of sufficient quality to allow comparison with theory an automated experiment is needed which can gather data of better than .3% statistical counting error over an interval of 2000 eV above the edge.

Experiments have shown EXAFS to be sensitive to the atomic structure about the absorbing atom. However, neither the experimental data nor previous theories have been sufficient

to make EXAFS more than an interesting phenomenon. In this thesis a new theory and improved data will be presented which not only show quantitative comparison between theory and experiment, but demonstrate that EXAFS can be used as a powerful new research tool to study the structure of amorphous material.

Chapter 2

Point Scattering Theory of X-ray K Absorption Fine Structure

Any successful theory will have to explain the following experimentally observed conditions: (1) EXAFS has been found in crystalline and non-crystalline solids, liquids, and polyatomic gases - everything except monatomic gases; (2) EXAFS is sensitive to the interatomic distances and the symmetry of the atoms surrounding the absorbing atom; (3) EXAFS is temperature dependent and becomes sharper at lower temperatures; and (4) EXAFS depends strongly on the symmetry of the electron that absorbs the x-ray. For instance, the L_{II} and L_{III} spectra which originate from p electrons are identical to each other but different from the L_I and K EXAFS which are identical and originate from s electrons.

In this chapter a simple, flexible theory of K edge absorption fine structure will be proposed which incorporates these observations. Although the physical mechanism responsible for EXAFS is the same for any sro theory and the result derived herein have elements which can be found in previous sro results,^{3,5-9} no previous calculation incorporates all of these necessary elements. There are also differences in the approximations that are made. This allows calculation of spectra which agree with the observed spectra in shape, position, and relative size of the peaks. The theory does not attempt to calculate an absolute value of the absorption coefficient but retains only those terms which yield an oscillatory behavior,

nor does it calculate the structure near the absorption edge (i.e., within 50 eV or so) which is affected by the singularity produced by the interaction of the photoelectron with the ionized atom,¹¹ and by the detailed scattering from surrounding atoms.

During an x-ray absorption event conservation of energy demands that the energy of the ejected photoelectron, E , be

$$E = h\nu - E_K \quad (2-1)$$

where $h\nu$ is the energy of the x-ray photon, E_K is the K shell binding energy, and it is assumed that the ion core is left in an unexcited singly ionized state. If I_0 is the intensity of the incident x-ray beam then the intensity of the beam transmitted through an absorber of thickness x is given by the familiar equation

$$I = I_0 e^{-\mu x} \quad (2-2)$$

or

$$\mu x = \ln \left(\frac{I_0}{I} \right) \quad (2-3)$$

where μ is the total linear attenuation coefficient. Experimentally I and I_0 are measured at a series of photon energies and $\ln(I_0/I)$ is plotted as a function of photoelectron energy. Any observed fine structure is attributed to oscillations in the linear attenuation coefficient. This coefficient is in turn related to the total attenuation cross section by

$$\mu/\rho = \sigma_T \quad (2-4)$$

where σ is the number density of atoms in the absorber and

$$\frac{\sigma}{T} = \frac{\sigma_A}{A} + \frac{\sigma_{sc}}{sc} \quad (2-5)$$

where σ_A is the photoelectric absorption cross section and σ_{sc} is the total scattering cross section. σ_{sc} will be ignored since it does not contribute to the oscillatory behavior. We consider only the photoelectric cross section, which may be written using the dipole approximation for radiative transitions ¹²

$$\sigma_A = 4\pi^2 \alpha h\nu |\mathbf{e} \cdot \mathbf{r}_{if}|^2 N(E) \quad (2-6)$$

where α is the fine structure constant, $N(E)$ is the density of final states, \mathbf{e} is the polarization vector of the x-ray, and \mathbf{r}_{if} is the dipole matrix element given by

$$\mathbf{r}_{if} = \int \phi_i(\mathbf{r}_1, \mathbf{r}_2, \dots, \mathbf{r}_N) \cdot \sum_n \mathbf{r}_n \cdot \phi_f(\mathbf{r}_1, \mathbf{r}_2, \dots, \mathbf{r}_N) d\tau \quad (2-7)$$

where ϕ_i and ϕ_f are the total many body wave functions of the initial and final atomic states.

To evaluate this matrix element we must estimate the many electron wave functions ϕ_i and ϕ_f which are given approximately by Slater determinants of one-electron wave functions,⁴ and $N-1$ of N electron states which are the same for the initial and final states. The discrete wave functions are assumed to be normalized to unity and the continuum functions normalized per energy interval. (A good discussion of the evaluation of this matrix element and the assumptions relating to it can be found elsewhere.^{12,13}) Many body effects are now included as approximations in the one electron wave functions which are solutions of the Hartree-Fock equation. However, some of the

effects of the hole in the K shell for energies below 50 eV are not included in the wave functions such as those that produce singularities at the edge¹¹. Since shielding can distort the wave function, particularly at energies near the K edge,¹¹ this theory is not expected to be reliable for photoelectrons of low energy. Under these assumptions the matrix element becomes

$$M = \int \psi^*(\mathbf{r}) \xi \psi_f(\mathbf{r}) d\tau \quad (2-8)$$

Variations in the absolute square of this matrix element are directly related to the x-ray absorption fine structure spectrum. In the case of K-shell absorption ψ_1 may be represented by the atomic 1-s wave function. ψ_f is the final photoelectron wave function including scattering and it is this wave function which must be found.

ψ_f is the state at a given energy which is the solution of the problem of a solid with an atom at the origin ionized by an electron missing from the K-shell while the surrounding atoms are neutral. We assume a muffin-tin-type potential -- a spherically symmetric potential about each atom with a radius which is smaller than half the distance between atoms with a constant potential outside in the rest of the solid. The ionized absorbing atom will have a different potential from that of the neutral atoms. We expect the potential of the ionized atom to be shielded by the surrounding conduction electrons justifying its assumed localized nature. The energies of interest are of the order of 50 eV or so greater than the Fermi energy. These energies are much greater than any of

the expected matrix elements of the pseudo-potentials or T-matrices that determine the scattering from the neutral atoms. For this reason the scattering should be weak and contributions which correspond to multiple scatterings from the neutral atoms can be neglected. Therefore, each neutral atom can be replaced by a delta function potential chosen to give the same back-scattered wave toward the ionized atom as would the actual neutral atom.

The ionized atom is more difficult to treat. It cannot be replaced by an effective potential since overlap of the initial and final state wave functions must be determined near the nucleus. Hence, the full problem must be solved with the complete potential. The variations in the x-ray absorption spectrum are produced by the interference near the nucleus between the outgoing wave from the absorbing atom and the waves backscattered from the surrounding neutral atoms. When these waves add constructively there is an absorption maximum and a minimum when they add destructively. The problem of solving the final state wave function inside the ionized atom will be delayed until the form of the wave function just outside of the ionized potential is considered (where the potential is constant). The wave function will have two parts, an outgoing wave corresponding to an electron excited from the K-shell and a part consisting of backscattered waves from the surrounding neutral atoms. The outgoing wave can be separated into radial and angular parts. In general, the radial part will have the form

$$R = N h_1^{\prime} (kr) \quad (2-9)$$

where

$$h_1^{\prime} (kr) = \exp (2i\eta_1) h_1^{+} (kr) \quad (2-10)$$

and N is a normalization constant assumed to be real, h_1^{+} is the outgoing Hankel function and may be visualized as an outgoing spherical wave relative to the ionized atom. The phase shift η_1 is introduced by the presence of the ionized atom at the origin and would be zero if there were no such atom present.

For K-shell absorption the initial electron state is an s state and the dipole selection rule [$\Delta l = \pm 1$ for the matrix element (eq. 2-8)] allows only transitions to states with p symmetry ($l = 1$). The total wave function will be the product of $h_1^{\prime} (kr)$ and a linear combination of the three spherical harmonics for $l = 1$ which represent the x, y, and z components of the wave function. These components will be considered one at a time starting with the z component. The spherical harmonic in the z direction is $y_1^0 = \cos\theta$, so that the wave function of the outgoing part of the photoelectron wave function is

$$\psi(r)_z = N h_1^{\prime} (kr) \cos\theta \quad (2-11)$$

To obtain the total wave function we must add the contribution from the scattered waves. This contribution is composed of the scattering from all of the surrounding atoms. As discussed previously, we are interested in the energy range where scattering from a single atom is small. We will therefore neglect the multiple scattering contribution, i.e., scattering from more than one atom. However, we will include

multiple scattering from the same atom which converts the potential matrix to the T-matrix. It is only the T-matrix which is small from an isolated atom. The scattered wave can now be calculated by¹⁴

$$\psi_{sc} = \sum_i (E - H_0 - A)^{-1} T(r_{\tilde{r}_i}) \psi_f^i \quad (2-12)$$

where $(E - H_0 - A)^{-1}$ is the Green's function of the average medium for energy E, through which the electron propagates. $T(r_{\tilde{r}_i})$ is the T-matrix of the neutral atom at \tilde{r}_i , and ψ_f^i is the incident wave at point r_i produced by all other neutral atoms excluding the atom at r_i and is given by

$$\psi_f^i = \psi + \sum_{m \neq i} (E - H_0 - A)^{-1} T(r_{\tilde{r}_m}) \psi_f^m \quad (2-13)$$

and A is an operator with only diagonal elements equal to n_{kk}^T defined by eqs. (2-16) and (2-17). In our approximation of small T-matrix ψ_f^i is independent of the atom at r_i and is equal to ψ_f . We replace $T(r_{\tilde{r}_m})$ by

$$T(r_{\tilde{r}_m}) = V_0 \delta(\tilde{r} - \tilde{r}_m) \quad (2-14)$$

with V_0 chosen to produce the same backscattered wave as produced by $T(r_{\tilde{r}_m})$. The equation we need to solve is, substituting $\psi_f^i = \psi_f$ and using eq. (2-14)

$$\psi_{sc} = V_0 \sum_i (E - H_0 - A)^{-1} \delta(\tilde{r} - \tilde{r}_i) \psi_f \quad (2-15)$$

It is important to note that ψ_f is significantly different from ψ . As ψ_f moves further from the origin more and more of the scattered waves from surrounding atoms are added to it and it deviates more from ψ . Sufficiently far from the origin ψ_f should be modified to the form of an eigenstate and produce no more scattered waves. In addition, electron-electron, and

electron-phonon scatterings make ψ_f lose coherence with ψ_f .

Thus, only the atoms within a certain distance of the origin contribute to the backscattering. An estimate of this scattering length will be given later. This effect is approximated by assuming that ψ_f decays exponentially away from the origin.

The scattering has two other effects. The scattering from

the periodic array of neutral atoms produces energy gaps corresponding to energy regions where no propagating states can occur. In these regions the E vs. k spectrum and the density of states are distorted from a simple free electron behavior. However, because the scattering is weak, the widths of the gaps are small, and, since the experimental data averages over several eV which is an energy interval large compared to the gaps, the gap effects should not be observable. For that reason we neglect the gap effects on the density of states, and assume that $N(E)$ varies as in a free electron gas, proportional to k . The scattering from the periodic array also changes the average k -value of ψ_f to k' . The equation determining this is

$$E - \frac{\hbar^2 k'^2}{2m} - n T_{k'k'} = 0 \quad (2-16)$$

where n is the number of neutral atoms per unit volume and $T_{k'k'}$

is the forward scattering amplitude given by

$$T_{k'k'} = \int \exp(-ik' \cdot \vec{r}) T(\vec{r}) \exp(ik' \cdot \vec{r}) d\tau \quad (2-17)$$

Equation (2-15) can be written as

(2-18)

$$\psi_{sc}(\vec{r}) = - \frac{V_0^{2m}}{4\pi\hbar^2} \sum_i \int \frac{\exp(ik'|\vec{r}-\vec{r}'|)}{|\vec{r}-\vec{r}'|} \delta(\vec{r}-\vec{r}_i) \psi_f(\vec{r}') d\tau$$

where the spatial representation of the Green's function has

been used and

$$E = \frac{\hbar^2 k^2}{2m} \quad (2-19)$$

As discussed above ψ_f is approximated by

$$\psi_f(r)_z = N h'_1(k'r) \cos\theta \exp(-\gamma r) \quad (2-20)$$

where k' is determined from eq.(2-26) and γ is a measure of the scattering length mentioned previously. Combining eqs.(2-18) and(2-20) we obtain

$$\psi_{sc}(r) = - \frac{V_0 2mN}{2\pi\hbar} \sum \frac{\exp(ik'|\mathbf{r}-\mathbf{r}_1|)}{|\mathbf{r}-\mathbf{r}_1|^2} h'_1(k'r_1)(z-z_1) \exp(-\gamma r_1) \quad (2-21)$$

where the fact that the cosine of the angle between \mathbf{r} and the z-axis is

$$\cos\theta_1 = \frac{(z-z_1)}{|k-r_1|} \quad (2-22)$$

and z_1 is the z-component of \mathbf{r}_1 has been used. The total wave function outside the ionized atom will be a combination of eqs. (2-11) and(2-21) giving

$$\psi_f(r) = N h'_1(k'r) \cos\theta - \frac{V_0 mN}{2\pi\hbar} \sum \frac{\exp(ik'|\mathbf{r}-\mathbf{r}_1|)}{|\mathbf{r}-\mathbf{r}_1|^2} h'_1(k'r_1) e^{-\gamma r_1} (z-z_1) \quad (2-23)$$

This expression for ψ_f is expected to be a reasonable approximation just outside the ionized atom. It remains to extrapolate this expression inside the ionized atom. This is done by using the WKB approximation with the Langer correction for the phase shift. This phase shift, introduced by the presence of the ionized atom, is given by¹⁶

(2-24)

$$n_1 = \int_{r_1}^{r_0} \left(k'^2 - \frac{2mV(r)}{\hbar^2} - \frac{2.25}{r^2} \right)^{1/2} dr - \int_{r_2}^{r_0} \left(k'^2 + \frac{2.25}{r^2} \right)^{1/2} dr$$

where r_1 and r_2 are the zeros of their respective integrands, $V(r)$ is the atomic potential, and r_0 is a point on the constant part of the muffin-tin-potential (assumed to be zero). In determining ψ near $r = 0$ this phase shift must be subtracted from the first term and added to the second term on the right side of eq. (2-23).

For the medium and heavy elements the 1-s function is sharply peaked near the origin and the p-wave can be approximated by a straight line passing through the origin, thus the amount of p-character in the wave should be closely approximated by the magnitude of the slope of this line. The matrix element eq. (2-8) will therefore be proportional to

(2-25)

$$\frac{M}{\hbar} \frac{\partial \psi_f(0)}{\partial z} = N \frac{\partial h_1^+(0) \cos \theta_0}{\partial z} - \frac{\exp(2i n_1) V_{mn}}{2\pi\hbar^2}$$

$$\times \frac{\partial}{\partial z} \left[\sum_i \frac{\exp(ik' |r-r_i|)}{|r-r_i|^2} h_1^+(k'r_i) \exp(-\gamma r_i) (z-z_i) \right]$$

or

(2-26)

$$\sum_i \frac{\exp(ik'r_i)}{r_i^2} h_1^+(k'r_i) \exp(-\gamma r_i)$$

$$x = \left(\frac{2z_i^2}{r_i^2} - 1 - \frac{ik'z_i^2}{r_i} \right)$$

$$\frac{\partial h}{\partial z}(0)$$

where A is a constant proportional to $\frac{1}{\partial z}$

The x-ray absorption cross section per unit energy is proportional to $|(\mathbf{e} \cdot \mathbf{M})|^2 k'$, where the k' comes from the density of final states eq. (2-6). Only the cross product in $|\mathbf{M}|^2$ contributes to the oscillatory fine structure spectrum. Therefore, the fine structure spectrum is proportional to

$$x = \operatorname{Re} \left[e_z^2 \exp(2in_1) V_o k' \sum_i \frac{\exp(ik'r_i)}{r_i^2} h_1^+(k'r_i) \exp(-\gamma r_i) \left(\frac{2z_i^2}{r_i^2} - 1 - \frac{ik'z_i^2}{r_i} \right) \right] \quad (2-27)$$

where $\operatorname{Re} []$ means the real part of the bracketed term. Using the relationship

$$h_1^+(kr) = -\exp(ikr) \left(\frac{i}{(kr)^2} + \frac{1}{kr} \right) \quad (2-28)$$

in eq. (2-27) we can write

$$x = e_z^2 V_0 k' \sum_i \frac{\exp(-\gamma r_i)}{k' r_i^3} \left[\left(\frac{2z_i^2}{r_i^2} - 1 \right) \alpha_i - \frac{k' z_i^2}{r_i} \beta_i \right] \quad (2-29)$$

where

$$\alpha_i = \frac{\sin[(2k')r_i + 2n_i]}{k' r_i} - \cos[(2k')r_i + 2n_i] \quad (2-30)$$

and

$$\beta_i = \frac{\cos[(2k')r_i + 2n_i]}{k' r_i} + \sin[(2k')r_i + 2n_i] \quad (2-31)$$

Equation (2-29) may be simplified by comparing the relative magnitudes of the separate terms and noting that experimentally k' varies from about 2 to 20 \AA^{-1} , while r varies from about 1.5\AA to 10\AA . Using these numbers and simplifying the notation by dropping the prime on k in eq. (2-29) reduces to

$$x \approx -V_0 k e_z^2 \sum_i \frac{\exp(-\gamma r_i)}{r_i^4} z_i^2 \sin[2kr_i + 2n(k)] \quad (2-32)$$

It now remains to calculate the fine structure contribution of the x and y components, however the task is considerably simplified by noting that both the derivation and the final expression (eq. 2-29) are invariant under rotation of the coordinate axes so

that the final answer may be written directly

$$x(k) = -V_0 k \sum_i \frac{\exp(-\gamma r_i)}{4} \sin(2kr_i + 2n(k)) \quad x \\ \left(e_z^2 z_i^2 + e_y^2 y_i^2 + e_x^2 x_i^2 \right) \quad (2-33)$$

This expression may now be evaluated for various crystal symmetries and polarization states of the incoming x-rays, however the case of interest is unpolarized x-rays so that $e_x^2 = e_y^2 = e_z^2 = 1/3$ which gives the final result

$$x(k) = -\frac{kV_0}{3} \sum_j N_j \frac{e^{-\gamma r_j}}{r_j^2} e^{-2\sigma_j^2 k^2} \sin(2kr_j + 2n_j) \quad (2-34)$$

where the sum is now over coordination shells, N_j is the number of atoms in the j^{th} shell, the term $\exp(-2\sigma_j^2 k^2)$ is a temperature term to be discussed later, and $x_i^2 + y_i^2 + z_i^2 = r_i^2$. Eq. (2-33) may also be evaluated for materials with cubic symmetry for any polarization of the x-rays. Since $x_i^2 = y_i^2 = z_i^2 = r_i^2/3$ for cubic symmetry, eq. (2-33) reduces to eq. (2-34) for this case also. EXAFS spectra calculated with this simplified expression eq.(2-34) have changes in peak positions of less than 1 eV and changes in amplitude of less than 2% from the spectra calculated with the complete equation eq.(2-29). The importance of the separate factors in this equation for calculating EXAFS spectra will now be discussed.

Note that the photoelectron wave vector k is not related to E by the simple free electron relation shown in eq. (2-19), but instead by eq. (2-16) where

$$nT_{kk} = (W_o - W) \quad (2-35)$$

and W is the work function and W_o is the average potential energy of an electron at rest between the atoms in a crystal.¹⁷ Since the experimental data is taken as a function of energy while the theoretical expression is a function of k it is important that a reliable method of calculating or determining W_o be found.

Kozlenkov⁸ has calculated W_o for a number of elements by averaging the atom's potentials over a unit cell of the crystal. Mott¹⁷ has developed a method in which he arbitrarily chooses W_o and references the experimental spectrum to this new energy scale. He then uses eq. (2-16) to find the value of the extrema, and finds the phase shifts of these extrema, and compares them to the WKB phase shifts he has calculated. This process is repeated with a new choice of W_o until the best fit with the calculated phase shift is obtained. For general application this method has the disadvantage that the WKB phase shifts may not be the best phase shifts to use. This depends on the choice of potentials and in many materials suitable solid state potentials are not known and other less satisfactory potentials must be used. Also the EXAFS that Mott measured originated primarily from the first coordination shell. In many materials the observed EXAFS has major contributions from several shells and it is difficult to sort out which

features belong to which shells over the entire range of the observed spectrum. On the other hand, calculations like those of Kozlenkov are tedious and are appropriate only for crystalline materials where the structure is known. This problem is related to the general uncertainty in the solid state potentials for the wide variety of materials which can be studied by EXAFS, i.e. elemental substances, alloys, and amorphous metals and semiconductors. If the potential is unknown then both the internal potential and the phase shift are uncertain and some method which finds the quantities self-consistently to obtain a "best" fit of eq. (2-34) to the observed spectrum must be found. For simple metals such as Cu and α -Fe reasonable potentials exist so that reliable phase shifts can be calculated. The inner potentials are usually reliable to within a few eV and a good fit to the observed EXAFS can be obtained by varying the value of the inner potential. This has the effect of shifting the energy scale by the amount of the variation and expanding or contracting the spectrum slightly by changing the periodicity of the sine waves in eq. (2-34). For more complicated materials a variational method similar to Mott's using just the nearest neighbor distance in eq.(2-34) can be used provided that reliable phase shifts and near neighbor distances are known. Although finding reliable values for $W_0 - W$ is essentially an unsolved problem for complex materials, the shapes of spectra calculated from reasonable estimates of this quantity are not sensitive to variations in W_0 (which only shifts the spectra and varies the positions of the extrema). This does not alter the basic correctness of our result.

The factor V_0 in eq. (2-34) is chosen to give the correct backscattering of the photoelectron. In backscattering the electron changes its wave vector by $2k$ and thus $V_0 \propto V(2k)$ the $2k^{\text{th}}$ Fourier component of the scattering potential. This, in turn, is related to the electron scattering factor, f , and henceforth the identification

$$V_0 = f(2k) \quad (2-36)$$

will be made, which is expected to be a reasonable approximation of the k dependence of the scattering. A qualitative understanding of the z dependence of the backscattering can be obtained from the following argument. Physically the backscattering must be due to scattering from the ion core in order to produce the needed large momentum transfers. The amount of penetration of the photo-electron into the ion core may be estimated by noting that back-scattering occurs from the charge within a region on the order of twice the wave length of the photoelectron (i.e. $d \approx \frac{2\pi}{k}$) around the scattering atom. The ionic charge that this represents can be estimated from

$$Z_{\text{eff}} = Z - n_{\text{eff}} \quad (2-37)$$

where Z is the atomic number of the atom and n_{eff} is the number of electrons within the radius d around the scattering atom. This may be estimated from the electronic structure of the particular atoms involved and the radii of the electronic shells given by Slater¹⁸. The result of these estimates for O, Ge, and Se for some typical values of k are given in Table 1.

TABLE 1

Data for Back-Scattering in O, Ge and Se

O	$k(\text{\AA}^{-1})$	E(eV)	d(\text{\AA})	z_{eff}	$f_o(k)$	$\frac{k^2 f(k)}{z_{\text{eff}}}$
	5	95	.63	1	3.8	95
	10	380	.31	5	2.4	48
	15	1520	.16	6	1.7	63

Ge	$k(\text{\AA}^{-1})$	E(eV)	d(\text{\AA})	z_{eff}	$f_o(k)$	$\frac{k^2 f(k)}{z_{\text{eff}}}$
	5	95	.63	4	9.7	60
	10	380	.31	13	8.0	62
	15	1520	.16	22	6.4	65

Se	$k(\text{\AA}^{-1})$	E(eV)	d(\text{\AA})	z_{eff}	$f_o(k)$	$\frac{k^2 f(k)}{z_{\text{eff}}}$
	5	95	.63	6	10.3	43
	10	380	.31	15	8.3	55
	15	1520	.16	24	6.7	63

E is the photoelectron energy for the listed values of k calculated from eq. (2-19). A comparison of the Z_{eff} and the scattering factors from Doyle and Turner¹⁹ are also given, and since the scattering from a point charge of Z_{eff} is expected to be

$$f(k) = 4\pi \frac{Z_{\text{eff}} e}{k^2} \quad (2-38)$$

then $k^2 f(k)/Z_{\text{eff}}$ should be approximately constant. It can be seen from Table 1 that the values of $k^2 f(k)/Z_{\text{eff}}$ particularly at higher energies are approximately constant and equal to about the same value for all atoms. This implies that $f(k)$ scales approximately as Z_{eff} as required by eq. (2-38). From Table 1 the values of Z_{eff} are roughly proportional to Z . This allows an average f to be defined, as a rough approximation for a multicomponent material, which is proportional to the average Z for the material. Although it is much better to use the tabulated $f(k)$'s for each component the present quality of the data is such that the general behavior of the backscattering can be described by an average $f(k)$.

The product $kf(2k)$ forms the envelope of the fine structure spectrum. In Fig. 2 the product $kf(2k)$ is compared for a free electron scattering factor, a screened coulomb scattering factor, and the self-consistent scattering factors of Doyle and Turner.¹⁹ All three curves give a similar behavior at high energies. At low energies the free electron factor diverges while the other two curves give a peak about $k = 4$ and fall to zero as $k \rightarrow 0$ which is better agreement with the observed EXAFS. Since the theory isn't

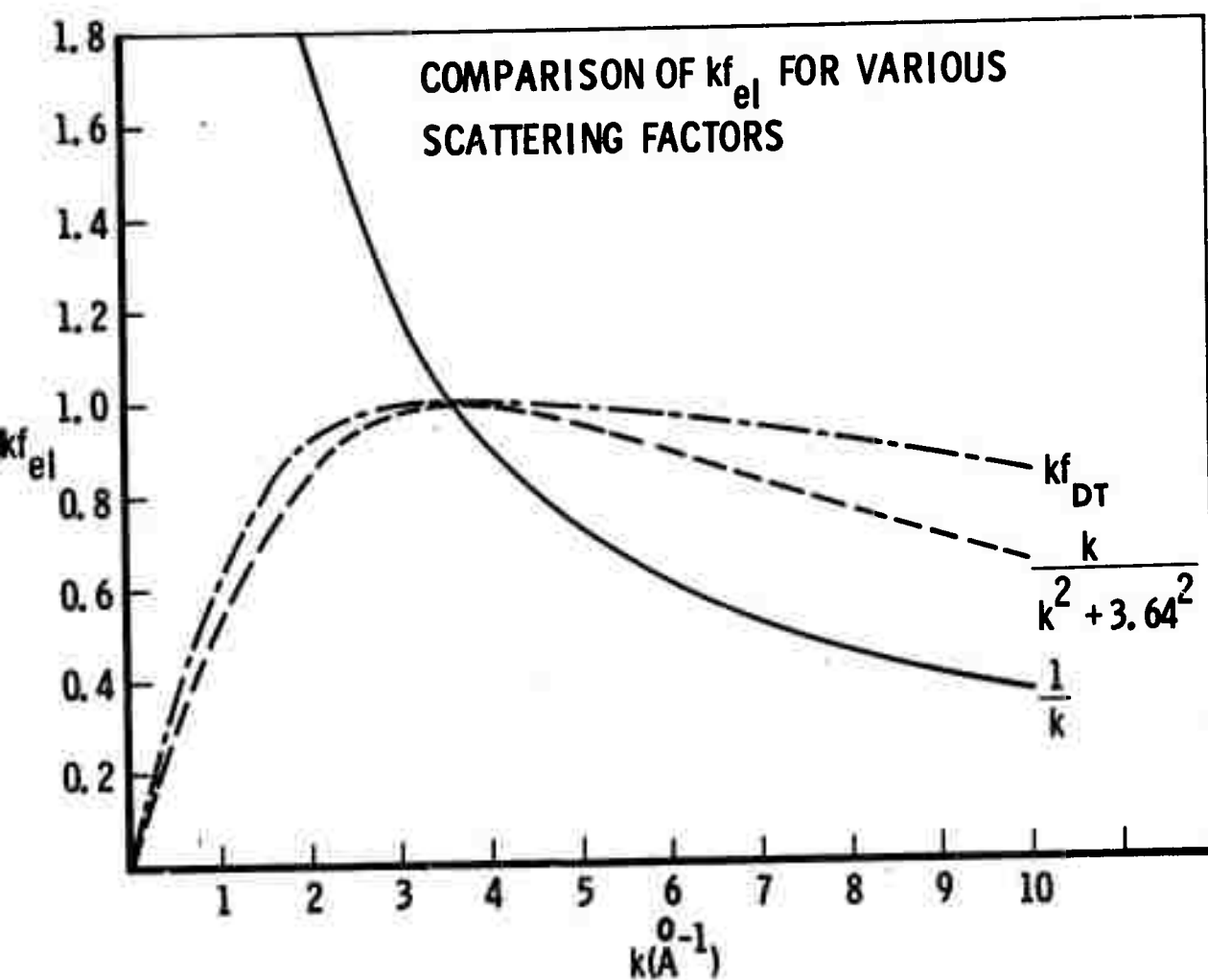


Figure 2

Comparison of the factor $kf(k)$ using (a) the free electron,
 (b) the screened coulomb, and
 (c) the Doyle and Turner scattering factors.

expected to be valid below about 50 eV, either scattering factor is acceptable. The scattering factors of Doyle and Turner are especially convenient since they are presented in terms of an expansion in a 4 term exponential series which lends itself to direct computer coding.

The range term $\exp(-\gamma r)$ in eq. (2-34) is similar in form to that used by Shiraiwa⁹. However, he attributed the range to inelastic scattering which is questionable since estimates of this scattering length are on the order of several lattice spacings for the photoelectron energies of interest. This is an apparent contradiction to experiment which shows only significant contributions from about two lattice spacings (~5 coordination shells). Instead we propose that the dominant operative as the photoelectron propagates farther and farther into the lattice is that the scattered waves from the surrounding atoms are added to the wave function and it becomes more like an eigenstate of the system, and therefore, produces no more coherently scattered waves. A rough estimate of this distance can be made as follows: The distance, d , that the photoelectron travels before it is scattered into an eigenstate of the system can be estimated from

$$d = \frac{\hbar k \tau}{m} \quad (2-39)$$

where τ is the time it takes to be scattered into an eigenstate and is not related to the usual lifetime due to inelastic scattering.

τ can be estimated by considering the expansion of the electron wave function of the solid

$$\psi(r,t) = \sum_n a_n \psi_n \exp\left(\frac{iE_n t}{\hbar}\right) \quad (2-40)$$

where the sum is over the states of the system which differ by reciprocal lattice vectors and is subject to the condition

$$\psi(r,0) = \exp(ik \cdot r) \quad (2-41)$$

Generally in a solid the two dominant states in the sum will be k and $k + g_1$ where g_1 is the shortest reciprocal lattice vector. Considering only these two states the phase term in eq. (2-40) is $\exp[i(E_{k+g_1} - E_k)t/\hbar]$. This may be rewritten using

the definition for the free electron energy eq. (2-19) and the fact that $k \gg g_{\min}$ for the electron energies of interest. Then

$$\exp\left[\frac{i(E_{k+g_1} - E_k)t}{\hbar}\right] \approx \exp\left[\frac{imkg_1 t}{m}\right] \quad (2-42)$$

When this argument is non-zero the plane wave term will be important and the other terms will partially cancel each other; however, when the argument of the exponential is π , all terms add directly and change the wave function to an eigenstate of the system. This gives an estimate of the time, τ .

$$\tau \approx \frac{m\pi}{\hbar kg_1} \quad (2-43)$$

In the case of copper which has a b.c.c. reciprocal lattice

$$g_1 = \frac{2\pi}{a} \sqrt{\frac{3}{2}} \quad (2-44)$$

Therefore, from eq. (2-39) and (2-44)

$$d = a/\sqrt{3} \quad (2-45)$$

or $d = 2.1\text{\AA}$ in copper. This mechanism dominates all other scattering mechanisms in determining the range over which the photoelectron backscattering contributes to EXAFS. The result is also independent of k for $k \gg g_1$. This argument identifies the range parameter γ as the reciprocal of the scattering length for scattering of the photoelectron into an eigenstate. Its accurate value is determined by a fit to experimental data for EXAFS and is typically about $\gamma = .3$. In Chapter 4, γ will be determined directly from the experimental data for crystalline germanium.

The term $\exp(-2\sigma_j^2 k^2)$ is a general Debye form for the temperature correction that must be applied because of the thermal motion of the lattice.

The origin of this term may be seen by the following simple derivation. If the thermal motion of all of the atoms in the solid is taken into account then the theoretical expression for EXAFS should be written

$$x(t) = -kf(k) \sum_i \frac{e^{-\gamma r_i}}{r_i^2} \sin(2kr_i(t) + 2n) \quad (2-46)$$

where $r_i(t)$ is the distance between the absorbing atom and the i^{th} atom, including the thermal motion of both atoms, and the sum is now over individual atoms. It is the time average of eq. (2-46) that is needed for EXAFS. If one typical sine term is considered

from the sum then the time averaged expression can be simplified by rewriting

$$\bar{r}_i(t) = \bar{r}_i^0 + \sigma_i(t) \quad (2-47)$$

where \bar{r}_i^0 is the equilibrium distance between the absorbing atom and the i^{th} atom and $\sigma_i(t)$ is the relative displacement of the atoms because of the thermal motion then we may write

$$\begin{aligned} \overline{\sin(2kr_i(t) + 2n)} &= \overline{\sin(2kr_i^0 + 2n)} \cos(\overline{2k\sigma_i(t)}) + \\ &\quad \cos(\overline{2kr_i^0 + 2n}) \overline{\sin(2k\sigma_i(t))} \end{aligned} \quad (2-48)$$

where the bars indicate time averaging. Since the displacements are random in sign and magnitude the time average of $\overline{\sin(2k\sigma_i(t))}$ will be zero so that

$$\overline{\sin(2kr_i(t) + 2n)} = \overline{\sin(2kr_i^0 + 2n)} \cos(\overline{2k\sigma_i(t)}) \quad (2-49)$$

the cosine term may be expanded as

$$\cos(\overline{2k\sigma_i(t)}) \approx 1 - \frac{(2k)^2}{2} \sigma_i^2(t) + \dots \quad (2-50)$$

but this can be related to

$$e^{-x^2} \approx 1 - x^2 + \dots \quad (2-51)$$

where

$$x^2 = 2k \sigma_1^2(t) \quad (2-52)$$

so that the expression for EXAFS becomes

$$x(t) \approx -kf(k) \sum_j \frac{N_j e^{-\gamma r_j}}{r_j^2} e^{-2k \sigma_j^2(t)} \sin(2kr_j + 2\eta) \quad (2-52)$$

where the sum is now over coordination shells and it is assumed $\sigma_j^2(t)$ is the same for all atoms in the coordination shell.

Although this derivation was simplified to show the origin of the temperature term in EXAFS; it can be made more rigorous and shown to be valid over a large temperature range^{21,22}. The shell to shell variation in σ can be seen by relating σ to the individual motion of the absorbing and scattering atom, as follows

$$\overline{\sigma_j^2(t)} = \overline{u_j^0(t)^2} + \overline{u_j(t)^2} - 2\overline{u_j^0(t) u_j(t)} \quad (2-54)$$

where $\overline{u_j^0(t)}$ and $\overline{u_j(t)}$ are the displacements of the absorbing and scattering atom along the equilibrium position vector and this expression is valid to order $\left(\frac{u_j}{r_j^0}\right)^2$.

If $\overline{u_j^0} = \overline{u_j}$ as expected in a monatomic material then eq. (2-54) shows that $\overline{\sigma_j^2} = 2\overline{u_j^2}$ for two atoms vibrating completely independently of each other (i.e. $\overline{u_j^0(t) u_j(t)} = 0$) while $\overline{\sigma_j^2} = 0$ for atoms whose motion is completely coupled.²⁰ (i.e. $\overline{(u_j^0(t) u_j(t))^2} = 2\overline{u_j^2}$).

An exact theory for the temperature dependence of any material depends on calculating $\overline{u_j^0(t) u_j(t)}$ for each shell which in turn depends on the structure and force constants in a material. This does emphasize that the temperature correction will be different for each shell in a material changing from a more coupled behavior in the first shell to the independent value in the higher shells.

The general behavior of u_j for different shells may be seen by writing the u_j 's in terms of the normal modes of the lattice, thus

$$\overline{u_i(m)} = \sum_{\xi, \sigma} a_\sigma(\xi) \{ \dot{u}_i(\xi) \exp(i\xi \cdot r(m)) \quad (2-55)$$

where σ is the index for the three phonon polarization modes, ξ is the phonon wave vector; a_σ is the amplitude of the normal mode $\{$ is the unit displacement vector for the mode, m is the mass of the atoms (monatomic material) and N is the number of atoms and the time average has been taken. Using eq. (2-55) we may write

$$\overline{u_i(m) u_i(n)} = \sum_{\substack{\xi, \sigma \\ \xi', \sigma'}} a_\sigma(\xi) \{_{i\sigma}(\xi) a^*_{\sigma'}(\xi') \{_{j\sigma}^*(\xi') \exp(i(\xi \cdot r(m) - \xi' \cdot r(n))) \quad (2-56)$$

Reproduced from
best available copy.

this expression is for one pair of lattice points. It must be averaged over pairs of lattice points separated by $r(m) - r(n)$ so that

$$\begin{aligned} \overline{u_i(m) u_i(n)} &= \frac{1}{2N} \sum_n \sum_{\substack{\xi, \sigma \\ \xi', \sigma'}} a_\sigma(\xi) \{_{i\sigma}(\xi) a^*_{\sigma'}(\xi') \{_{i\sigma'}^*(\xi') \\ &\times \exp(i\xi \cdot r_{mn}) \exp(i(\xi - \xi') \cdot r(n)) \end{aligned} \quad (2-57)$$

where $\tilde{r}_{mn} = \tilde{r}(m) - \tilde{r}(n)$, but

$$\sum_n \exp(i(\kappa - \kappa') \cdot \tilde{r}(n)) = N\delta_{\kappa, \kappa'}, \quad (2-58)$$

so that eq. (2-57) becomes

$$\overline{u_1(m)u_1(n)} = \frac{1}{2} \sum_{\kappa, \sigma} |a_\sigma(\kappa)|^2 \exp(i\kappa \cdot \tilde{r}_{mn}) \quad (2-59)$$

where we've used the fact that $\{\tilde{r}\}$ is a unit vector and that if $\kappa = \kappa'$ then $\sigma = \sigma'$ since the modes are independent. Eq. (2-59) and (2-54) may now be combined to give

$$\overline{\sigma_j^2} = \sum_{\kappa, \sigma} |a_\sigma(\kappa)|^2 (1 - \exp(i\kappa \cdot \tilde{r}_{mn})) \quad (2-60)$$

At this point we start approximations. Let us assume the Debye approximation where the energy of a mode depends only on the magnitude of κ for a given σ . It then follows that $a_\sigma(\kappa)$ depends only on the magnitude of κ . By changing the sum over κ to an integral and doing the integral over angles

$$\overline{\sigma_j^2} = 4\pi \frac{V}{(2\pi)^3} \sum_\sigma \int_0^\infty |a_\sigma(\kappa)|^2 \left(\frac{1 - \sin \kappa r_{mn}}{\kappa r_{mn}} \right) \kappa^2 d\kappa \quad (2-61)$$

where κ is the maximum phonon wave vector; and V is the volume of the solid. The amplitude of the normal waves can be expressed in terms of the energy of the wave using the usual expression for the harmonic oscillator

$$|a_\sigma(\kappa)|^2 = \frac{2\hbar}{mN\omega(\kappa)} (n + \frac{1}{2}) \quad (2-62)$$

where n is the Bose-Einstein distribution given by

$$n = \left(\exp\left(\frac{\hbar\omega(\kappa)}{k_B T}\right) - 1 \right)^{-1} \quad (2-63)$$

thus eq. (2-61) becomes

$$\sigma_j^2 = \frac{1}{N} \frac{V}{2\pi^2} \frac{2\hbar}{m} \int_0^{\infty} [(e^{\hbar\omega/k_B T} - 1)^{-1} + \frac{1}{2}] \left(1 - \frac{\sin \kappa r_{mn}}{\kappa r_{mn}} \frac{\kappa^2}{\omega(\kappa)} \right) d\kappa \quad (2-64)$$

This expression can be evaluated further using the Debye approximation

$$\omega = v\kappa$$

where v is an average of the transverse and longitudinal velocities.

For the behavior at $T = 0$ (where $n=0$) then from eq. (2-65) eq. (2-64) may be evaluated

$$\sigma_j^2 = \frac{1}{N} \frac{V}{4\pi^2} \frac{\hbar\kappa^2 D}{mv} \left[1 + \frac{2}{\kappa_D^2 r_{mn}^2} [\cos(\kappa_D r_{mn}) - 1] \right] \quad (2-66)$$

For high temperatures $n + \frac{1}{2} \rightarrow k_B T/\hbar\omega$ so that eq. (2-64) becomes

$$\sigma_j^2 = \frac{1}{N} \frac{2V}{2\pi^2} \frac{k_B T \kappa}{mv^2} D \left[1 - \frac{Si(\kappa_D r_{mn})}{\kappa_D r_{mn}} \right] \quad (2-67)$$

where Si is the usual sine integral.

The second term in the brackets in both eq. (2-66) and eq. (2-67) comes from the cross term in eq. (2-54) and both go to zero as $r \rightarrow \infty$. These results agree with Schmidt^{21,22} in the two temperature limits. Schmidt extends the calculations for the intermediate temperatures of interest for EXAFS.

He proposes that the EXAFS temperature correction for the j^{th} shell be of the form $\exp(-I_j)$ where

$$I_j = \frac{12 \hbar^2}{k_B m \theta_D} k^2 \phi_j(T/\theta_D) \quad (2-68)$$

and k_B is the Boltzman constant, m is the mass of the atoms in the absorber, θ_D is the Debye temperature of the absorber, k is the wave vector of the photoelectron, and

$$\phi_j(T/\theta_D) = \phi_{1j} \frac{T}{\theta_D} + \phi_{2j} \frac{\theta_D}{T} + \phi_{3j} \left(\frac{\theta_D}{T}\right)^3 \quad (2-69)$$

where ϕ_{1j} , ϕ_{2j} , and ϕ_{3j} are defined in reference 22 and depend only on the crystal structure of the absorber. All data presented herein were taken at liquid nitrogen temperature ($T = 77.4^\circ K$). For these materials $T/\theta_D \sim .2$ while Shmidt suggested that eq. (2-68) is valid for $T/\theta_D \sim .33$. However, there is little difference in the calculated EXAFS between the correction from eq. (2-68) or the result derived in ref. 22 which is valid for $T \ll \theta_D$, so that eq. (2-68) was used as it was somewhat easier to evaluate. It should be noted that the temperature factor from eq. (2-68) cast in a general Debye form that can be used in eq. (2-34) by making the identification

$$\sigma_j^2 = \frac{6 \hbar^2}{k_B m \theta_D} \phi_j(T/\theta_D) \quad (2-70)$$

so that the differences in coupling coefficients are related to the differences in ϕ for each shell. In materials such as amorphous semiconductors where there is no method to calculate the thermal smearing for each shell, it would be possible in theory to measure EXAFS as a function of temperature and fit the variations to a Debye function. Experimentally this has been done for some crystalline materials^{23,24,25,26}, but it is usually difficult to separate out the shell to shell differences. Thus, the attempts at experimentally determining the temperature variation have met with little success. In the next chapter it is shown how structural information can be obtained directly from EXAFS, and it is suggested how an experimental measurement of the temperature variations will be possible. Finally, in the amorphous materials there is also a contribution to the average displacement of an atom about its equilibrium position because of structural disorder. Thus σ has both static and dynamic contributions which must be separated in any structural analysis. This will also be discussed in Chapter 3.

As mentioned the phase shift, $\eta(k)$, was calculated using the WKB method from eq. (2-24). The self-consistent Hartree atomic potentials of Herman and Skilman²⁷ were used for all calculations. These atomic potentials will be shielded in the solid and will not have as large a tail as that given by Herman and Skilman, thus providing an error in η . An additional error is introduced by the fact that the potential of the ionized atom differs from that given by Herman and Skilman because of the missing K shell electron. Further error is introduced by the WKB approximation. For these

reasons the calculations of n are not expected to be accurate enough to give detailed agreement with the experiment, although one expects semi-quantitative agreement. We use the WKB method as a tentative example of phase shift determination. The final values of n were determined from the experimental data and then used to calculate the fine structure. This was done as follows: The primary peak positions were assumed to come from the first coordination shell. The energy positions of these peaks were used to calculate the phase shifts for these energies using eq. (2-34). This was done for various choices of T_{KK} in eq. (2-16), and the results compared to the phase shift curve determined from the WKB approximation. The WKB curve and the experimentally determined curve for germanium are shown in Fig. 3. This technique is similar to methods used by Kozlenkov⁹ and by Mott¹⁷, and it underlines the close relationship between the atomic potential, the inner crystalline potential, and the phase shift. If the proper potentials aren't known, then k and n must be determined self-consistently by comparing the result of eq. (2-34) to the experimental EXAFS. We also emphasize that more suitable trial potentials than from Herman and Skilman may be found for some materials; however, the Herman and Skilman potentials represent a convenient starting point for all atomic species studies by EXAFS, especially since the phase shift is most sensitive to the potential of the type of absorbing atom and not on its crystal structure, bonding state, or kinds of neighbors (e.g., the phase shift of Ge in crystalline Ge, GeO_2 and GeSe are found to be the same to within

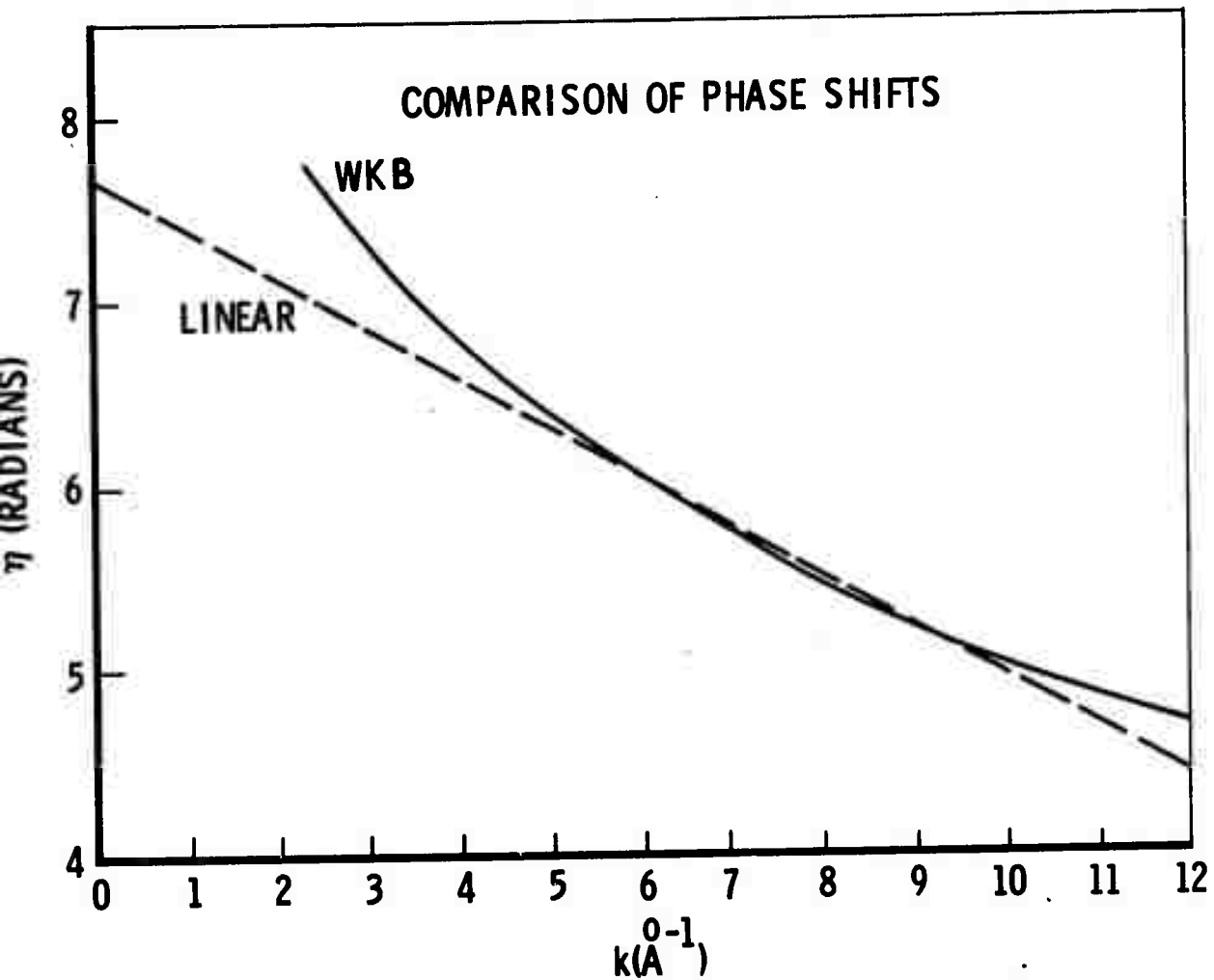


Figure 3

Comparison of the WKB phase shift using the Herman-Skillman potential and the fitted linear phase shift for Ge.

experimental error).

Theoretical EXAFS was calculated using eq. (2-34) for Cu (f.c.c. lattice), α -Fe (b.c.c.) and Ge (dia. cubic) and compared to experiment. The data used for each element are listed in Table II where $W_0 - W$ from eq. (2-35), $\eta(k)$, θ_D , and the constant factor in the temperature correction (eq. 2-55) are listed along with the values of N , r , and σ for thirteen coordination shells. The phase shifts are linear of the form

$$\eta = -ak + b \quad (2-71)$$

It has been found that summing to thirteen coordination shells is sufficient to include all shells which give a significant contribution to the fine structure. The summation of eq. (2-34) has also been performed to include 20 shells and no significant change in EXAFS was observed.

In Fig. 4a and b comparison of the theoretical and experimental EXAFS of Cu and Fe is shown. The theoretical curves are calculated using eq. (2-34) and the data of Table II. The experimental curves were from well-annealed foils of 2.5μ and 6μ thickness for Cu and Fe respectively. The data were all taken at $77^\circ K$. These curves are the oscillatory part of the absorption coefficient, corresponding to the definition of χ in eq. (2-34). The sloping background of the absorption coefficient has been subtracted graphically. A comparison of the curves shows very good agreement in the position, shape and relative heights of the EXAFS features over the entire experimental range. Below 100 eV there is a disagreement in the heights of the features because the

Table II

Input Data to Calculate EXAFS in Cu, Fe, and Ge

	Cu	Fe	Ge
	fcc	bcc	dia. cubic
a =	3.67 Å	2.85 Å	5.65 Å
k =	263(E+10) ^a	.263(E+15) ^a	.263(E-1) ^a
n =	-.245k + 7.95	-.194k + 7.96	-.267k + 7.60
γ =	.3	.3	.3
θ _D =	320°K	410°K	370°K
12k ² /k _B mθ _D ^b =	.02648	.02515	.02149
Shell, j =	N _j r _j /a φ _j ^b	N _j r _j /a φ _j ^b	N _j r _j /a φ _j ^b
1	12 0.707 .2333	8 0.866 .2098	4 0.433 .1694
2	6 1.000 .2800	6 1.000 .2355	12 0.707 .2624
3	24 1.225 .2809	12 1.414 .2598	12 0.829 .2723
4	12 1.414 .2797	24 1.658 .2570	6 1.000 .2708
5	24 1.581 .2838	8 1.732 .2566	12 1.096 .2698
6	8 1.732 .2904	6 2.000 .2601	24 1.225 .2724
7	48 1.871 .2960	24 2.208 .2664	16 1.299 .2758
8	6 2.000 .2992	24 2.236 .2672	12 1.414 .2819
9	36 2.121 .3003	24 2.249 .2676	24 1.479 .2850
10	24 2.236 .3002	32 2.598 .2740	24 1.581 .2882
11	24 2.345 .2998	12 2.828 .2740	12 1.639 .2890
12	24 2.449 .2998	48 2.958 .2736	8 1.732 .2893
13	72 2.550 .3005	30 3.000 .2735	24 1.785 .2890

a) The zero of energy is taken to be the Fermi energy. This definition of k is taken from eq. (2-16) and (2-35)

b) From ref. 21 and 22 and eq. (2-68) and (2-69)

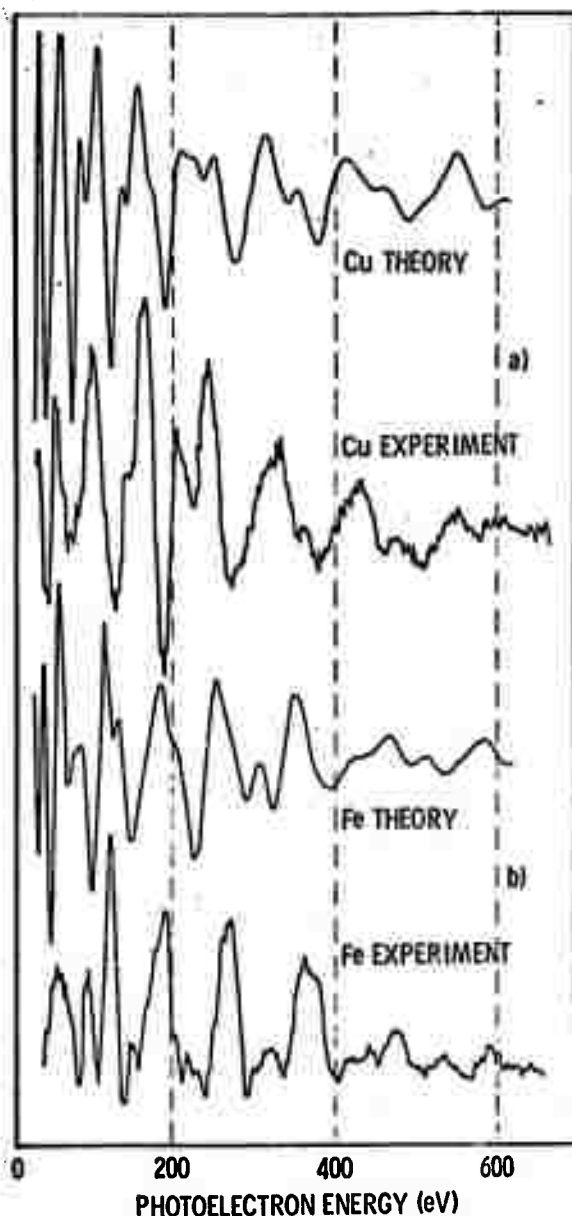


Figure 4

Comparison of theoretical and experimental EXAFS for copper and iron. The theoretical spectrum is obtained from eq. (2-34) and the data of Table II.

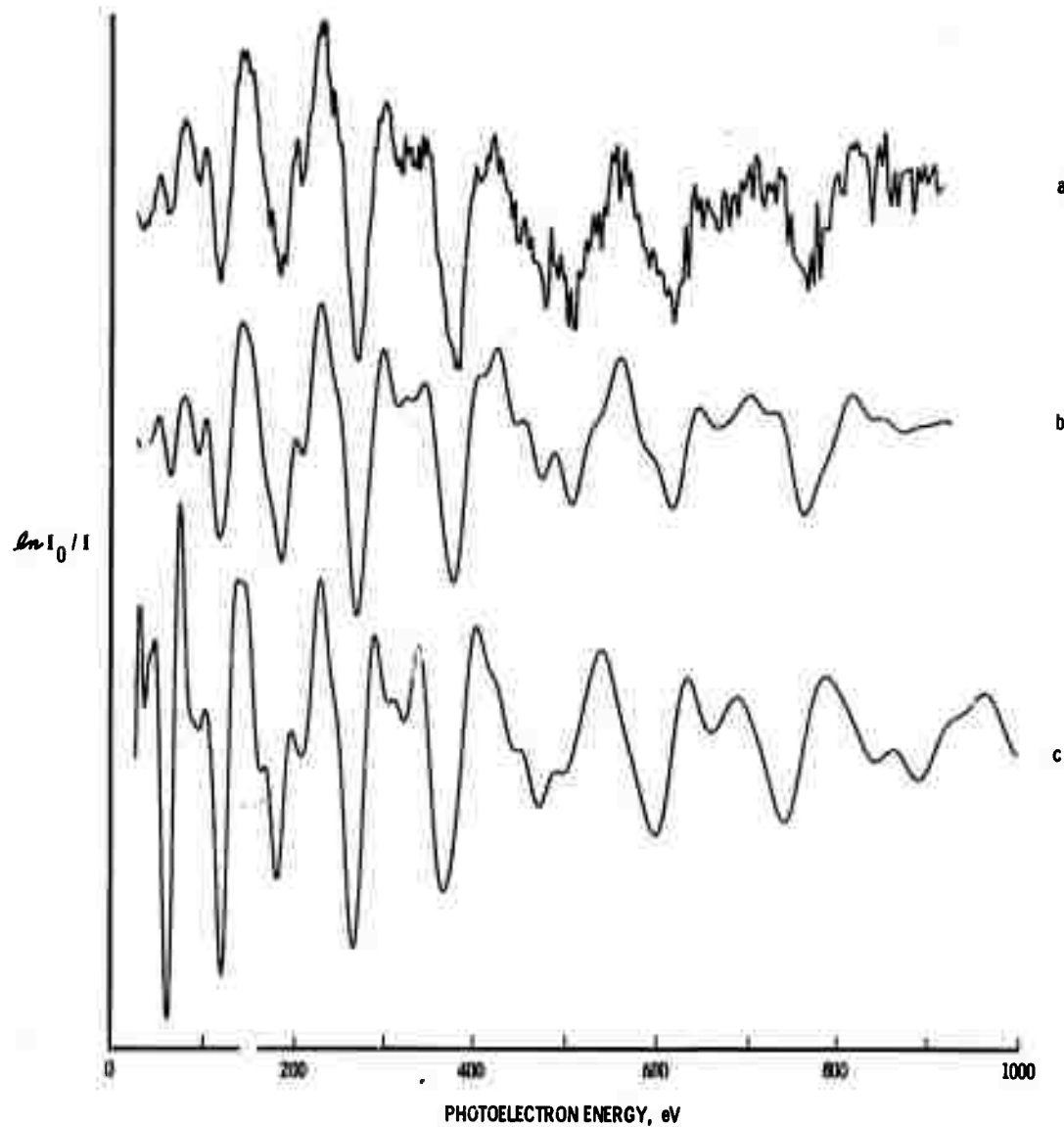


Figure 5

Comparison of theoretical and experimental EXAFS for germanium.

Curve (a) is the experimental data with the usual photoelectric edge removed, curve (b) is the smoothed experimental curve, and curve (c) is the theoretical curve calculated from eq. (2-34) and the data of Table II.

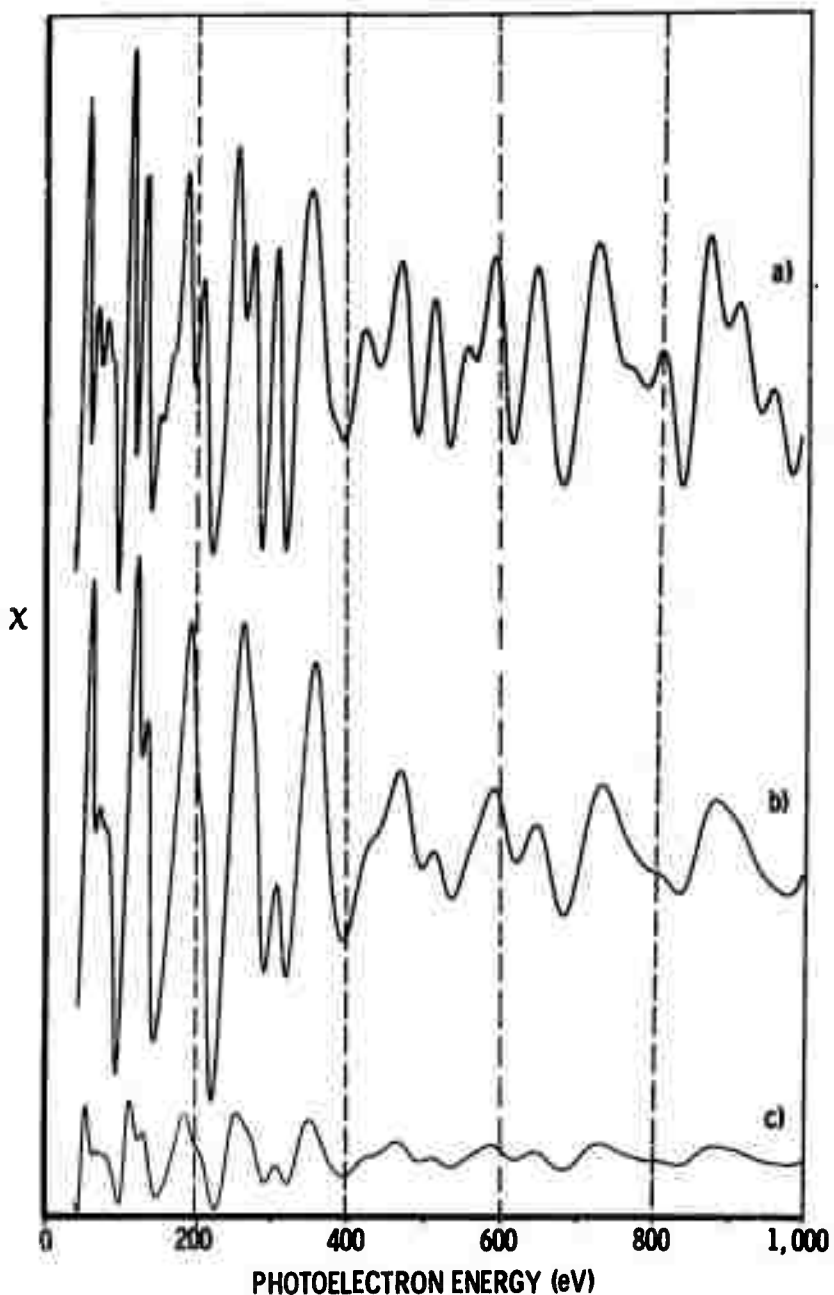


Figure 6

(a) Theoretical EXAFS for iron without the temperature and range terms, (b) temperature correction has been applied to curve (a), (c) the exponential attenuation has been applied yielding the theoretical curve in Fig. 4b. All curves are plotted to the same (arbitrary) scale.

scattering factor used in eq. (2-34) was not adequate. There is also some disagreement in shape, at the lower energies around 50 eV, but as mentioned previously the approximations made were not expected to be valid in this range.

In Fig. 5 a comparison of the theoretical and experimental EXAFS for germanium is shown. Curve (a) is the oscillatory part of the experimental absorption coefficient including statistical noise. Curve (b) is a smoothed version of Curve (a) where the statistical noise was filtered out using a computer method which will be described in Appendix A, and Curve (c) is the theoretical curve calculated from eq. (2-34) using the data of Table II. The agreement between the theoretical and experimental spectra is excellent over the entire range. Even below 100 eV there is general agreement with the position of the maxima, although the heights of the peaks in the theoretical spectrum are too large, which as mentioned above, may be due to the inadequate scattering factor used at the lower energies, the neglect of band effects on the density of states, or that the experimental resolution of 4-6 eV was not included in the calculated spectrum. This would have the effect of smoothing and reducing the features and would be most effective at the lower energies where the widths of the features are only a few eV wide.

In Fig. 6 the importance of the temperature and range terms in calculating EXAFS which agree with the experimental data is shown. Curve (a) is the curve for iron from Fig. 4b without the temperature or the range term. Curve (b) is the same as Curve (a) except the temperature factor from eq. (2-68) is applied. In

Curve (c) the range term is also applied, yielding the theoretical curve of Fig. 4b. The importance of both corrections in lowering the amplitudes of the peaks especially at higher energies and in smoothing the spectrum by reducing the contributions of higher coordination shells can be easily seen. It is obvious why earlier attempts^{8,9} to make quantitative comparisons of the theoretical and experimental data without applying these corrections met only limited success.

The computer program used to calculate theoretical EXAFS from eq. (2-34) is listed in Appendix C.

Chapter 3

A New Method for Structure Analysis Using The Fourier Transform of EXAFS

In Chapter 2 a simple, flexible theory of EXAFS was presented which allows calculation of fine structure spectra which are in good agreement with observed spectra. Perhaps of more practical interest is the inverse problem of determining the atomic arrangements in the material from its EXAFS; this would constitute a new and valuable research tool. The results of the point scattering theory (eq. (2-34)) showed that EXAFS was given by a sum of damped sine waves each originating from a coordination shell. This suggested that the data could be inverted using Fourier analysis.

If eq.(2-34) is rewritten

$$-\chi(k)k^{-1}f(k)^{-1} = \sum_j \frac{N_j e^{-\gamma r_j}}{r_j^2} e^{-2\sigma_j^2 k^2} \sin(2kr_j + 2n(k)) \quad (3-1)$$

the Fourier transform of this equation is

$$-\sqrt{\frac{2}{\pi}} \int_0^\infty \chi(k)k^{-1}f(k)^{-1} \sin(2kr+2n)dk = \\ \sum_j \frac{N_j e^{-\gamma r_j}}{8r_j^2 \sigma_j^2} e^{-\frac{(r-r_j)^2}{2\sigma_j^2}} + \Delta(r) = \phi(r) \quad (3-2)$$

Here $\Delta(r)$ is a function which is sharply peaked about $-r_j$ and is very small in the space $r > 0$ of physical interest and will be neglected from now on. The right hand side of eq. (3-2), $\phi(r)$, is a radial structure function. It shows that the transform of the experimental data, given by the left hand side of eq. (3-2), is a series of normalized Gaussian curves whose amplitudes are

$$A_j = \frac{N_j e^{-\gamma r_j}}{8r_j^2 \sigma_j} \quad (3-3)$$

and whose widths W_j , where the amplitude is down from its peak value to A_j/e are

$$W_j = 2\sqrt{2}\sigma_j \quad (3-4)$$

Note that in crystalline materials the atoms in a coordination shell will be exactly at r_j and the σ_j 's determined from the data using eq. (3-4) are entirely thermal in origin. For simple materials such as Fe, Cu and Ge, the measured σ_j 's can be compared to the σ_j 's calculated from Shmidt's theory^{21,22}. In more complex materials the widths of the Gaussians can be measured for each shell as a function of temperature, and fitted to Shmidt's theory or a similar function. This could be used to determine a Debye temperature for the material.

For structure analysis in crystalline materials the σ_j 's can be measured or calculated and, since the N_j 's and r_j 's are known from the crystal structure, the range parameter γ can be determined from the measured amplitudes A_j using eq. (3-3). This can be seen by rearranging eq. (3-3),

$$-\ln \frac{A_j}{(N_j / 8r_j^2 \sigma_j)} = \gamma r_j \quad (3-5)$$

Thus, plotting the left side of eq. (3-5) vs. r_j yields a straight line whose slope is γ . This will be done in Chapter 5 for Ge. It must be emphasized that this method is the only reliable way to determine the value of γ . Other calculations of γ are only approximate.

Another parameter that can be obtained from the radial structure function of crystalline materials is the phase shift. In deriving eq. (3-2), it was assumed that the phase shift was known and included in the argument of the analyzing waves. Often, however, the phase shift is not known sufficiently well to do this; thus, the argument of the analyzing wave used is $2kr$ instead of $(2kr + 2\eta)$. The result of the theory given by the right hand side of eq. (3-1) contains the phase shift which is assumed to have the linear form given by eq. (2-71) so that when the Fourier integration is done the right hand side of eq. (3-2) remains the same except that the argument of the exponential is now $(r - (r_j - a))^2$, where a is the k dependent part of the phase shift. This has the effect of shifting all of the peaks toward the origin by an amount a , where a is usually less than .4 so that $a \ll r$ in all cases. From the known distances of the coordination shells in a given crystal structure, the amount of the shift can be determined for that particular element. Once the k dependence of the phase shift is known, the constant part of the phase shift can be determined from the experimental data. Depending on how the

transform is taken it may not be necessary to know b to invert the data however, it is convenient to have to generate the linear phase shift so that EXAFS can be calculated using eq. (2-34) or the phase shifts for the same kinds of atoms in different materials can be compared. Finding b is done by locating the extrema of the peaks due to the dominant shell (usually the first shell) and using the equation for the extrema of the sine wave

$$\frac{2k}{n} \left(\frac{r_j - a}{j} \right) + 2b = (2n + 1) \frac{\pi}{2} \quad (3-6)$$

where a and b are the phase shift parameters from eq. (2-71), k_n is the k value of the n^{th} extremum, and $n = 0, 2, 4, \dots$ for maxima and $1, 3, 5, \dots$ for minima. Since the absolute value of n isn't known, eq. (3-6) can be solved for b using successive pairs of extrema and a "best" b is determined from the result.

In noncrystalline materials the problem of determining information is much more difficult since there is no reliable way of measuring or calculating parameters such as η , γ , and σ in these materials. Furthermore the peak width σ contains both static (disorder) and dynamic (thermal) broadening. If Gaussian shapes are assumed for both contributions to the width, then

$$\frac{\sigma_{\text{TOT}}^2}{j} = \frac{\sigma_T^2}{j} + \frac{\sigma_D^2}{j} \quad (3-7)$$

where T and D stand for thermal and disorder respectively. Hence, for a given shell σ_D , N_j and the kinds of atoms in a shell are all the important structural information. One method to obtain structural information from non-crystalline materials is to compare the non-crystalline radial structure function to the

function from its crystalline polymorph. If the short range order is similar in the two materials, then the assumption is made that the range parameter γ is the same in both the crystalline and non-crystalline material. This should be true if the near neighbor environment is similar in both materials and $1/\gamma$, the mean free path, is on the order of the inter-atomic spacing. It is also assumed that thermal smearing for similar shells is the same because of the similarity of the bonding involved. For any new peaks appearing in the amorphous structure function this assumption would be questionable, but this would be most serious only for the first one or two shells since beyond that the shell to shell variation in σ is only a few percent. Finally, it is assumed that the phase shift for the two polymorphs is the same since it has been found to depend primarily on the potential of the absorbing atom and not on the surrounding structure.

These assumptions make it possible to obtain structural information from the measured height and width using eqs. (3-3) and (3-4) with the crystalline values of γ and σ_j^T , and the following argument shows that absolute numbers of atoms in each shell may be determined from the data. Even though the theory does not predict an absolute value of the EXAFS cross section, it is expected that it is in error only by an overall multiplicative constant since all of the functional dependence was included in the theory. One method to obtain numbers of atoms directly from the data is to normalize the observed jump in both the crystalline and amorphous materials of the absorption coefficient at the K edge to the same (arbitrary) value. This in effect normalizes the

cross section for absorption in each material, so that the overall constant for both the crystalline and non-crystalline materials should be the same. If the cross sections have been normalized, then the results of the theory state that the relative amplitude of the observed fine structure from a given shell will be proportional to the number of atoms in that shell in the two materials. To get a quantitative comparison of number of atoms in a shell, the transforms of the two materials should be compared using eq. (3-3). The overall constant missing from eq. (3-3) should be the same and so the absolute values of the A_j 's obtained from the data can be used to obtain the number of atoms in an amorphous shell if the number of atoms in the comparable crystalline shell is known, using

$$\frac{N_j(A)}{N_j(C)} = \frac{A_j(A)\sigma_j(C)}{A_j(C)\sigma_j(A)} \frac{r_j(C)^2}{r_j(A)^2} \frac{e^{-\gamma r_j(A)}}{e^{-\gamma r_j(C)}} \quad (3-8)$$

In many amorphous materials the first shell is very similar to the first crystalline shell because the near neighbor bonding is the same, so that $r_j(A) = r_j(C)$ and $\sigma_j(A) = \sigma_j(C)$. Therefore a simplified form of eq. (3-8) may be used to find $N_j(A)$.

$$N_j(A) = N_j(C) \frac{A_j(A)}{A_j(C)} \quad (3-9)$$

Once N_j is known for any shell in the amorphous material, all of the other N_j 's can be determined by comparing the amplitude of their shells to the shell where N is known and applying eq. (3-3). Thus, even though absolute absorption data isn't taken, the EXAFS technique provides a straightforward method of determining the number and distribution of atoms about a given distance in most amorphous materials.

The preceding discussion of the kinds of structural information obtainable from EXAFS data was based in part on the fact that the integration in eq. (3-2) was over all k space. In fact, the EXAFS data is taken only over a small domain in k space which typically is from $k \approx 2$, because the data near the edge often contains features from effects other than EXAFS, to $k \approx 20$, which is the practical experimental limit, since the time involved to go farther would be prohibitive. When a Fourier transform is made over a finite range a termination error is introduced into the radial structure function. The corresponding problem in radial distribution analysis has been discussed by Warren²⁸ who shows that this error reduces the heights of the peaks, broadens them somewhat, and introduces a set of ripples on either side of the peak. Because the precise effect of the termination error in radial distribution analysis is given by a complicated convolution integral²⁸, the data is usually corrected for termination error by either applying an exponential convergence factor which reduces the ripples²⁸, or by a complicated iterative procedure designed to experimentally subtract the termination ripple from the data²⁹,

or by using analytic continuation of the data³⁰ to extend the range of the data and thereby reduce the termination effects.

The effect of termination error on the transform of EXAFS data is shown in Fig. 7, where the theoretical Ge EXAFS spectra of Fig. 5c has been transformed using eq. (3-2), except that the upper limit of integration is $k_m = 15$. As is evident from the figure there is some ripple introduced about each peak as a result of the transform.

One difference in the EXAFS termination error from that of radial distribution analysis is that the effect of termination can be evaluated by direct integration. The integral of interest is

$$I = \frac{1}{\sqrt{2\pi}} \int_0^{k_m} e^{-\alpha_j^2 k^2} \cos 2k\Delta r_j dk \quad (3-10)$$

where $\alpha_j = \sqrt{2\sigma_j}$, $\Delta r_j = r - r_j$, and k_m is the maximum value of k as determined by the range of data used in evaluating the integral from the left hand side of eq. (3-2). The integral (3-10) is the term giving the series of Gaussians in the region $r > 0$. The other term which would have given peaks about $r = -r_j$ may still be ignored since, even with termination effects, it will have no appreciable effect for $r > 0$. The integrand from (3-10) may be rewritten using

$$\cos x = \frac{1}{2} (e^{ix} + e^{-ix}) \quad (3-11)$$

giving

$$I = \frac{e^{-(\Delta r_j^2/\alpha_j^2)}}{2\sqrt{2\pi}} \left(\int_0^{k_m} e^{-(\alpha_j^2 k^2 + i\Delta r_j/\alpha_j)^2} dk + \right. \quad (3-13)$$

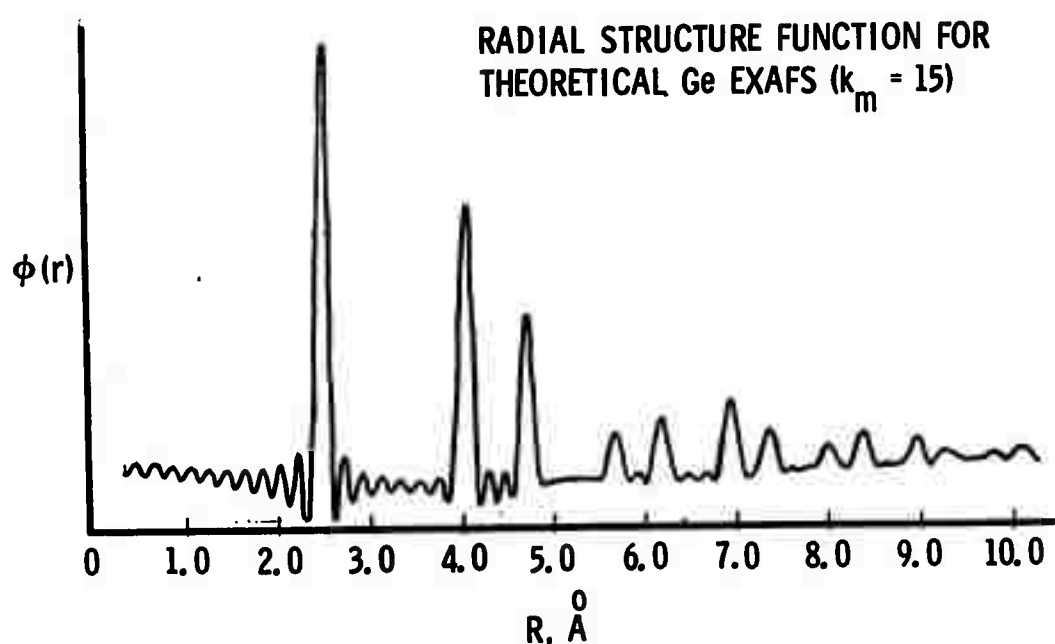


Figure 7

Termination effects on the radial structure function of the theoretical Ge EXAFS of Fig. 5c. ($k_m = 15$).

$$\int_{-\infty}^{\infty} e^{-(\alpha_j k - i\Delta r_j/\alpha_j)^2} dk \Big)$$

where the same k independent term used to complete the square has been factored from both integrals. These integrals may be evaluated in terms of error functions after changing the variables to $x_1 = \alpha_j k + i\Delta r_j/\alpha_j$ and $x_2 = \alpha_j k - i\Delta r_j/\alpha_j$

∴

$$I = \frac{e^{-(\Delta r_j^2/\alpha_j^2)}}{2\alpha_j \sqrt{2\pi}} \left(\int_{-\frac{i\Delta r_j}{\alpha_j}}^{\frac{\alpha_j k_m + i\Delta r_j}{\alpha_j}} e^{-x_1^2} dx_1 + \right) \quad (3-14)$$

$$\int_{+\frac{i\Delta r_j}{\alpha_j}}^{\frac{\alpha_j k_m - i\Delta r_j}{\alpha_j}} e^{-x_2^2} dx_2 \Big)$$

Thus,

$$I = \frac{e^{-(\Delta r_j^2/\alpha_j^2)}}{4\sqrt{2} \alpha_j} \left(\operatorname{erf}\left(\frac{\alpha_j k_m + i\Delta r_j}{\alpha_j}\right) + \operatorname{erf}\left(\frac{\alpha_j k_m - i\Delta r_j}{\alpha_j}\right) \right) \quad (3-15)$$

where the error functions from the bottom terms have cancelled since $\operatorname{erf}(-x) = -\operatorname{erf}(x)$. This expression may be reduced even further by using the expansion of an error function of complex argument given in Abramowitz and Stegun³⁰, so that

$$\begin{aligned}
 I &= \frac{e^{-(\Delta r_j^2/\alpha_j^2)}}{2\sqrt{2}\alpha_j} \left(\operatorname{erf}(\alpha_j k_m) + \frac{e^{-\alpha_j^2 k_m^2}}{2\pi\alpha_j k_m} (1 - \cos 2k_m \Delta r_j) \right. \\
 &\quad \left. - \frac{2e^{-\alpha_j^2 k_m^2}}{\pi} \sum_{n=1}^{\infty} \frac{e^{-n^2/4}}{n^2 + 4\alpha_j^2 k_m^2} (2\alpha_j k_m - 2\alpha_j k_m \cosh n\Delta r_j/\alpha_j) \times \right. \\
 &\quad \left. \cos 2k_m \Delta r_j + n \sinh n\Delta r_j/\alpha_j \sin 2k_m \Delta r_j \right) \tag{3-16}
 \end{aligned}$$

Although this expression is complicated, several factors are important. First, unlike radial distribution analysis, where the effect of termination is described by a convolution integral, here, the termination error merely multiplies the Gaussian curve. Secondly, the peak amplitude (at $\Delta r_j = 0$) is reduced by a factor of $\operatorname{erf}(\alpha_j k_m)$, where typically $\alpha_j k_m \approx 1$. Away from the peak the termination introduces a ripple of periodicity, π/k_m .

A comparison of the termination error that is calculated using eq. (3-16) versus the error obtained from direct integration is shown in Fig. 8. The parameters for the original Gaussian are shown in the figure and correspond to the first shell of Ge. The expression containing termination ripple calculated from eq. (3-15) is shown in curve b and the first shell curve obtained from direct integration as in Fig. 7 is shown in curve c. The reduction in amplitude and the broadening of the peak expected from eq. (3-15) are shown in the figure where a comparison of curves b and c show good agreement between the calculated and integrated result. The

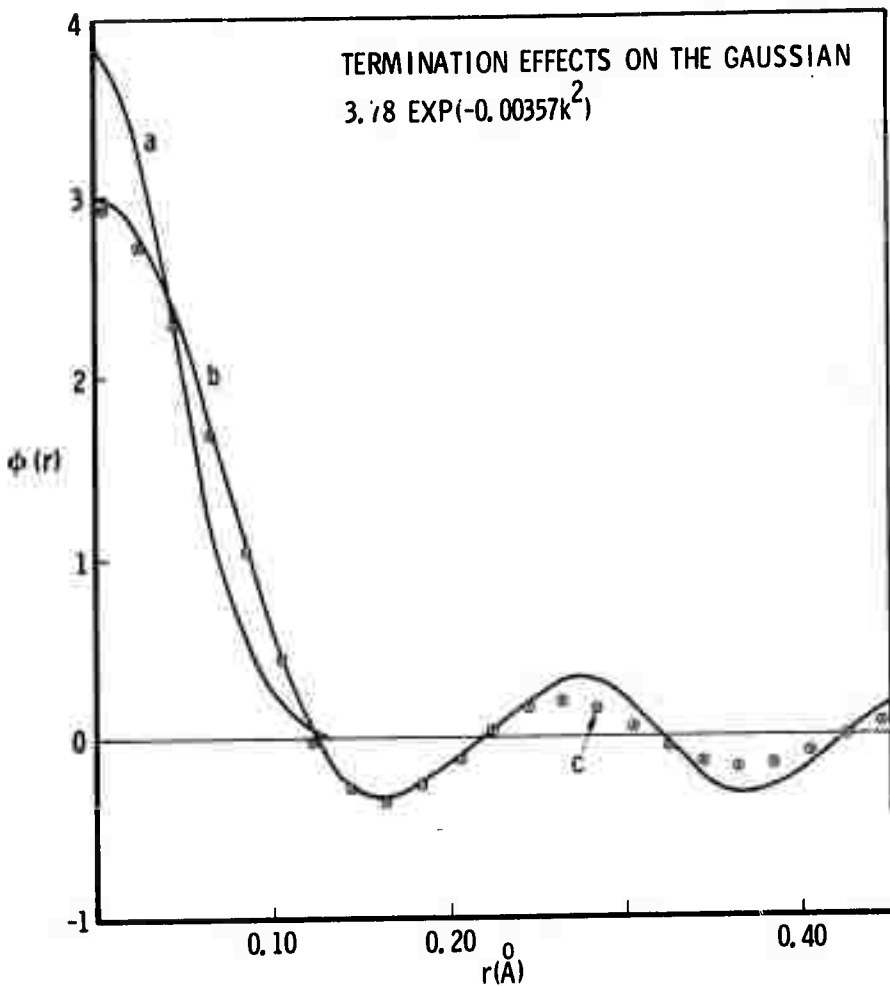


Figure 8

- (a) First shell Gaussian from the theoretical Ge rsf,
- (b) calculated termination effect using eq. (2-15) for $k_m = 15$,
- (c) termination effects on (a) from direct integration with $k_m = 15$.

differences between b and c above .25 \AA are the result of an approximation used in evaluating eq. (3-15) in this region. Unfortunately, the presence of statistical noise in the data and interpolation between data points during the integration routine has made it impossible to use eq. (3-15) to correct the actual experimental data for termination error. The results of this equation can be used to obtain the height and width of the Gaussians without termination for the major peaks, but it cannot be used to identify or correct small peaks whose amplitudes are on the order of the noise. These peaks are important in the study of non-crystalline materials and future work should develop techniques which will remove or reduce the termination effects and allow the resolution of small signal peaks from the data.

One final point should be made about comparing the data obtained from the EXAFS technique versus the data obtained from radial distribution analysis. The resolution possible in any transform atom of scattering or EXAFS data depends on the number of oscillations the various shells contribute over the range of the data. If EXAFS results are compared to any other method of determining radial distribution functions (x-ray, electron, or neutron scattering), and the data are taken over the same range of k space, the scattering intensity data varies as $\sin kr$, and the EXAFS data varies as $\sin 2kr$. Thus, there are twice as many oscillations in the EXAFS data, hence twice the resolution in the transformed data will be possible.

Chapter 4

Experimental Methods

In this chapter the experimental methods for obtaining EXAFS data are described. Although many techniques have been used throughout the years to record fine structure spectra the results have generally been of limited value because of the poor resolution and counting statistics, limited energy range above the absorption edge, and/or very slow data collection. The system described here permitted automated collection of medium resolution data with good counting statistics over energy intervals up to 2 keV above the absorption edge. All of this was necessary to obtain useful structural information from the Fourier transform of the data.

The basic x-ray system was a Siemen's Crystalloflex 4 power supply and horizontal single-crystal diffractometer. The x-ray continuum radiation from medium to heavy target tubes, such as W, Ag, and Mo, were operated at their highest power levels (usually 40 kV and 30 mA) for maximum intensity. To achieve adequate resolution, precise alignment of the spectrometer was obtained using narrow slits (usually 50 μ). The analyzing crystal used was a carefully selected single crystal of LiF ($2d_{200} = 4.0265\text{\AA}$) mounted in a holder which allowed accurate placement and alignment of the crystal in the beam. The x-rays were detected by a NaI (Tl) scintillation counter with a pulse height analyzer to eliminate higher order reflections, and recorded on a scaler/timer operated in a fixed count mode to assure good counting statistics for each data point.

Usually the time to accumulate 10^5 counts ($\sim .3\%$ statistical counting error) was measured. The numerical resolving power of the spectrometer, which corresponds to an energy resolution of 4-6 eV was $\lambda/\Delta\lambda \sim 2000 - 3000$.

The sample was mounted in a cryostat and suspended in the beam between the entrance slit and analyzing crystal on a holder beam which can automatically be moved in and out of the x-ray beam. The technique for doing this is illustrated in fig. 9. The sample holder was spring loaded to return to one position and actuated by means of a cam in contact with the center rod. The total excursion was controlled by mechanical stops with the sample holder isolated from the cryostat by a flexible bellows. The cam was activated by a connecting rod connected about 1" off center on the shaft of a Slo-Syn motor in a bell-crank arrangement. The rod was alternately pulled and released by rotating the shaft 180° each time the sample was to be moved. As the Slo-Syn shaft was rotated in the same direction each time, a separate system of cams and microswitch actuated a stepping motor driving the x-ray goniometer. The goniometer could be stepped in increments of $.0025 - .025^\circ$ depending upon the requirements of the experiment. Normal step sizes were $.005^\circ$ or $.010^\circ$. A schematic diagram of the apparatus is shown in fig. 10.

During a typical experimental run the goniometer was positioned at a fixed starting angle and the absorber positioned out of the beam. When 10^5 counts had been accumulated a signal was sent from the scalar to a Hamner Scanner-Coupler which held

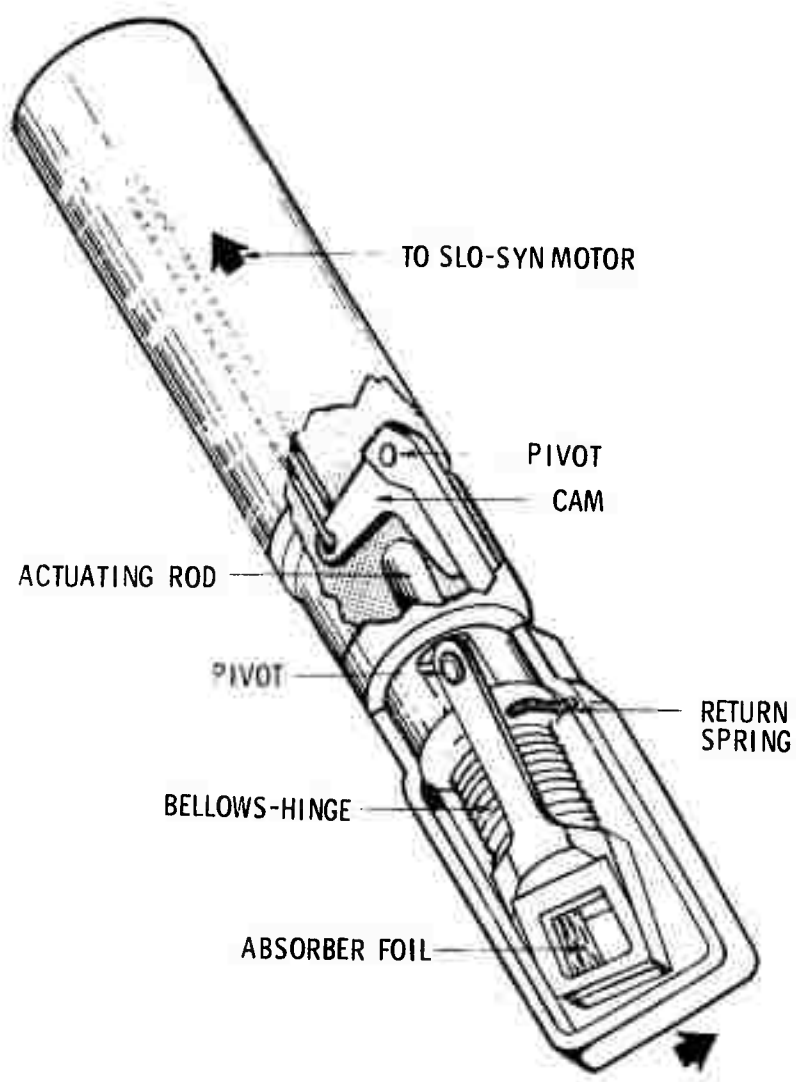


Figure 9

Diagram of the sample changing mechanism.

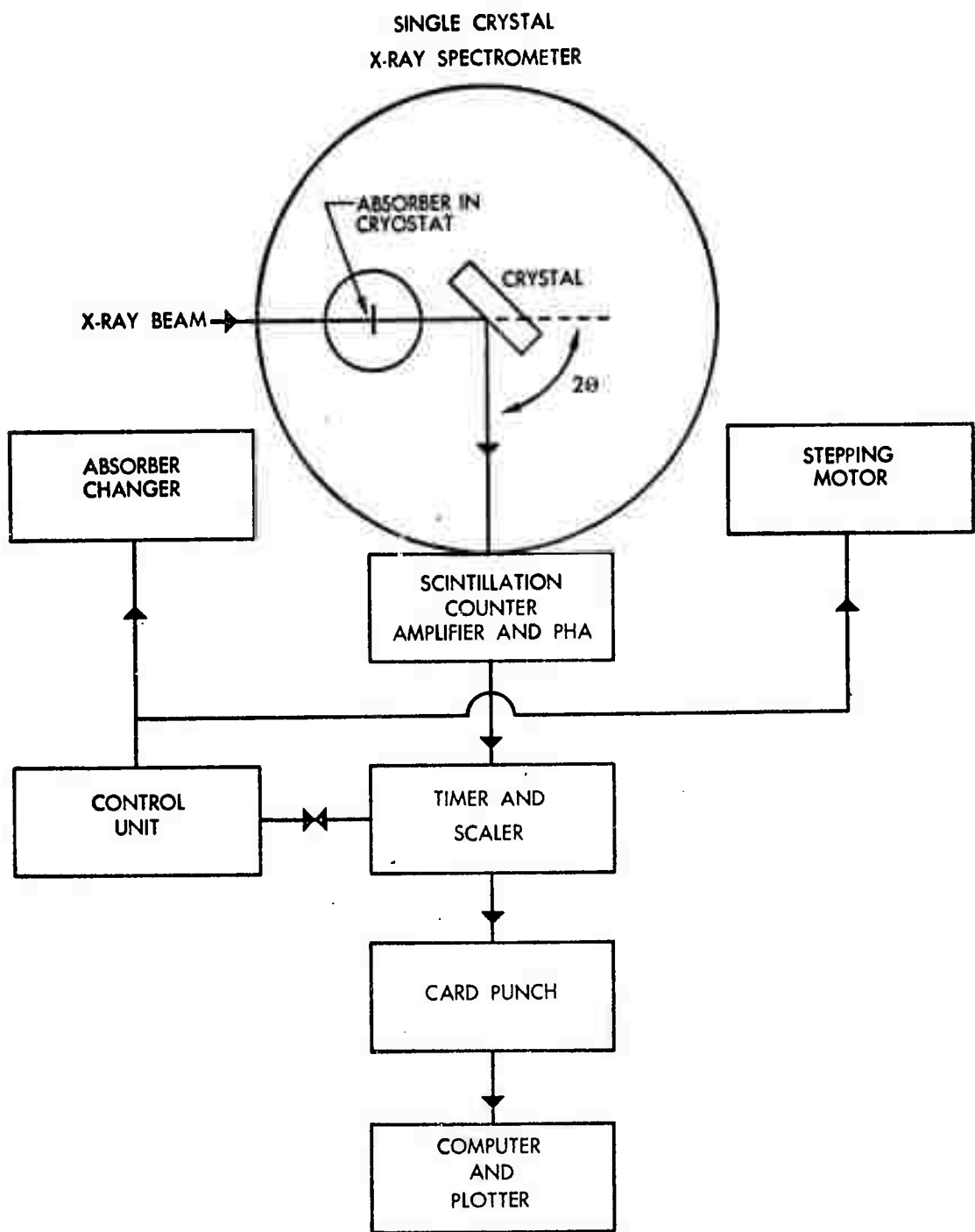


Figure 10

Schematic of the experimental apparatus.

the counting sequence, signaled a Humphrey Stepper Controller to rotate the Slo-Syn motor repositioning the sample, and relayed the digital information to an IBM keypunch which punches the accumulated time. This process was then repeated with the absorber in the beam. Each time the sample changer returned to its original position the goniometer was stepped by .005°. This process was automatically repeated until the entire region above and through the absorption edge was recorded. Typically, a run extended from 100 eV below the edge to 1500-2000 eV above the absorption edge. This corresponded to about a 4°20 range in the energy regions usually studied.

In order to obtain structural information using the method described in Chapter 3 the thermal smearing of the data must be minimized, which was done by taking most data at liquid nitrogen temperature (77°K). Although the cryostat was capable of operating down to 4°K, the small reduction in the thermal motion over that at 77°K was not worth the added effort and expense. Another requirement for adequate data was that the noise level be reduced so that signal could be extracted from the data as far from the edge as possible to obtain greater resolution and lessen Fourier termination effects. The major contribution to the noise was due to the statistical counting fluctuations. Although 10^5 counts limits the statistical fluctuations in the measured absorption cross-section to ~.3%, it must be remembered that the signal of interest was the small

oscillation on top of the usual photoelectric cross-section. 10^5 counts was the practical limit for the number of counts collected for each point because of long term drift in the experimental apparatus. Improved statistics were achieved by gathering data from several runs, usually 10 or more, and averaging them together. This was done since the noise was random and the starting points of the data were well aligned. This process was time consuming since each run took about 1 day. However, the final statistical fluctuations were $\sim .1\%$ which allowed resolution of the signal over a few hundred eV more range.

The data cards collected from each run were analyzed by a series of computer programs. The first program checked for errors that may have occurred during the experimental run. Typically the errors were mechanical and caused an I or I_o point to be missed. To keep the (I, I_o) pairs in proper order, values for the missed I or I_o were estimated and inserted.¹¹ This was not a serious problem occurring no more than 2 or 3 times per run.

All of the corrected data decks from a given sample were then combined into a single data deck. The careful alignment necessary was done by using the characteristic tube lines and W impurity lines present in the data. There were usually several of these lines in the data which allowed alignment of all of the decks to $\sim .0025^\circ$ which reflects the uncertainty of the initial positioning of the spectrometer.

The combined data deck was then analyzed by the main program which computes $\ln(I_0/I)$ and the energy scales from the angular data. The program also made internal corrections of the energy scale based on the positions of the impurity lines whose energies were known³² and corrected for the coincident losses when intense impurity lines appeared in the data. This program also had the capability to Fourier analyze the data using the fast Fourier transform (fft) described in Appendix A. The purpose of the analysis at this point was to remove the fine structure data from the total spectrum. Filtering out the lowest frequency from the transformed data and then retransforming the data accomplished this task. This method of extracting the fine structure data was preferred because of the simplicity of the technique. Since the shape of the photoelectric spectrum was not accurately known near the edge, a complicated fitting program would be required for each edge in order to find the correct background spectrum to remove from the data. The fft program was also used to filter out much of the statistical noise in the data to produce curves as in fig. 5b. This was done only to make comparisons easier; when the data was transformed to obtain structural information, the statistical noise was left in.

Proper sample preparation was also very important to obtain high quality EXAFS. Samples must be of uniform thickness over an area of about 1cm by 2.5cm. The metal samples were rolled into thin foils of about $2-20\mu$ thickness. The

optimum thickness depended on the absorption coefficient of the material but, empirically, it was observed that when $I_0/I \sim 3$ just above the absorption edge, the best resolution was obtained. For alloys and compounds the situation was more complicated; but, in general, the absorption jump was made sufficiently large so that the fine structure, whose amplitude at most was a few percent of the absorption jump, could be resolved. The rolled foils were well annealed to remove any effects of work hardening. Other materials were crushed into a fine uniform powder, mixed in Duco cement, and then thin layers were spread on Al foil. (The Al foil is 1 mil thick and used as a backing for thermal contact with the sample holder, but had a low absorption coefficient with no fine structure in the energy range of interest (5-20 keV).) Care must be taken to make uniform samples with no inhomogeneities or pinholes. Several of these thin layers were used to make uniform samples of optimum thickness. Some materials which were difficult to roll or grind and many amorphous samples were evaporated in vacuum onto 1 mil Al foil or mylar to a thickness of $\sim 1\mu$. Multiple layers were used for optimum thickness.

Chapter 5

Application of EXAFS Technique to Structure Determination

of Amorphous Ge, GeO_2 , and GeSe

In this chapter the techniques for structure determination using EXAFS will be applied to three amorphous materials--Ge, GeO_2 , and GeSe. The analysis of the amorphous samples is effected by standardizing the EXAFS parameters with their respective crystalline polymorphs, as described earlier.

The techniques to reduce the effect of termination errors have not yet been incorporated in the data analysis programs; therefore, the information from the peak widths is unreliable. Considerable structural information can be derived from only the positions and amplitudes of the peaks.

A. Germanium

Amorphous Ge was the first system studies with the EXAFS technique. It has been studied extensively by other techniques, since it is a simple, easily prepared amorphous system. The basic structural unit is the tetrahedron formed from Ge making 4 covalent bonds. In crystalline Ge adjacent tetrahedra are all linked in the staggered configuration which generates the diamond cubic lattice. In amorphous Ge the linking of the tetrahedra is not as regular leading to the breakdown of long-range order. Two primary explanations have been offered to describe the structure of amorphous Ge. The first was by Grigorovici and Manaila^{33,34}

who pictured the structural unit as a pentagonal dodecahedron made of 12 five-fold rings of linked eclipsed Ge tetrahedra. Fig. 11 shows the staggered and eclipsed linking of Ge tetrahedra. Their proposed structure consists of a 50-50 mixture of 5 fold rings and distorted crystalline regions, all linked together. Although this hypothetical structure is in general agreement with the experimental radial distribution function (r.d.f.), particularly in the reduction of the third peak, there is no detailed agreement and the density appears to be too low. Generally, the structure is somewhat artificial and the requirement that only staggered or eclipsed configurations be allowed is too rigid for a random structure.

A more recent model has been proposed by Polk³⁵ based on the continuous random network proposed by Zachariasen³⁶. Polk constructed a model to satisfy local bonding requirements, and minimize strain and surface density of unsatisfied bonds. He concluded that his 440 atom model could be extended indefinitely without postulating regions of special bonding. The r.d.f. calculated from his model agrees very well with the r.d.f. of amorphous Si by Moss and Graczyk³⁷ and the r.d.f. of amorphous Ge by Shevchik³⁸ which show the first and second peak at the crystalline distances and a small third neighbor peak at a slightly larger distance than in the crystalline case. In Polk's model the tetrahedral bond angle was shown to deviate $\pm 10^\circ$ about the ideal angle of $107^\circ 26'$ and the rotations of the tetrahedra about the common bond contained intermediate positions in

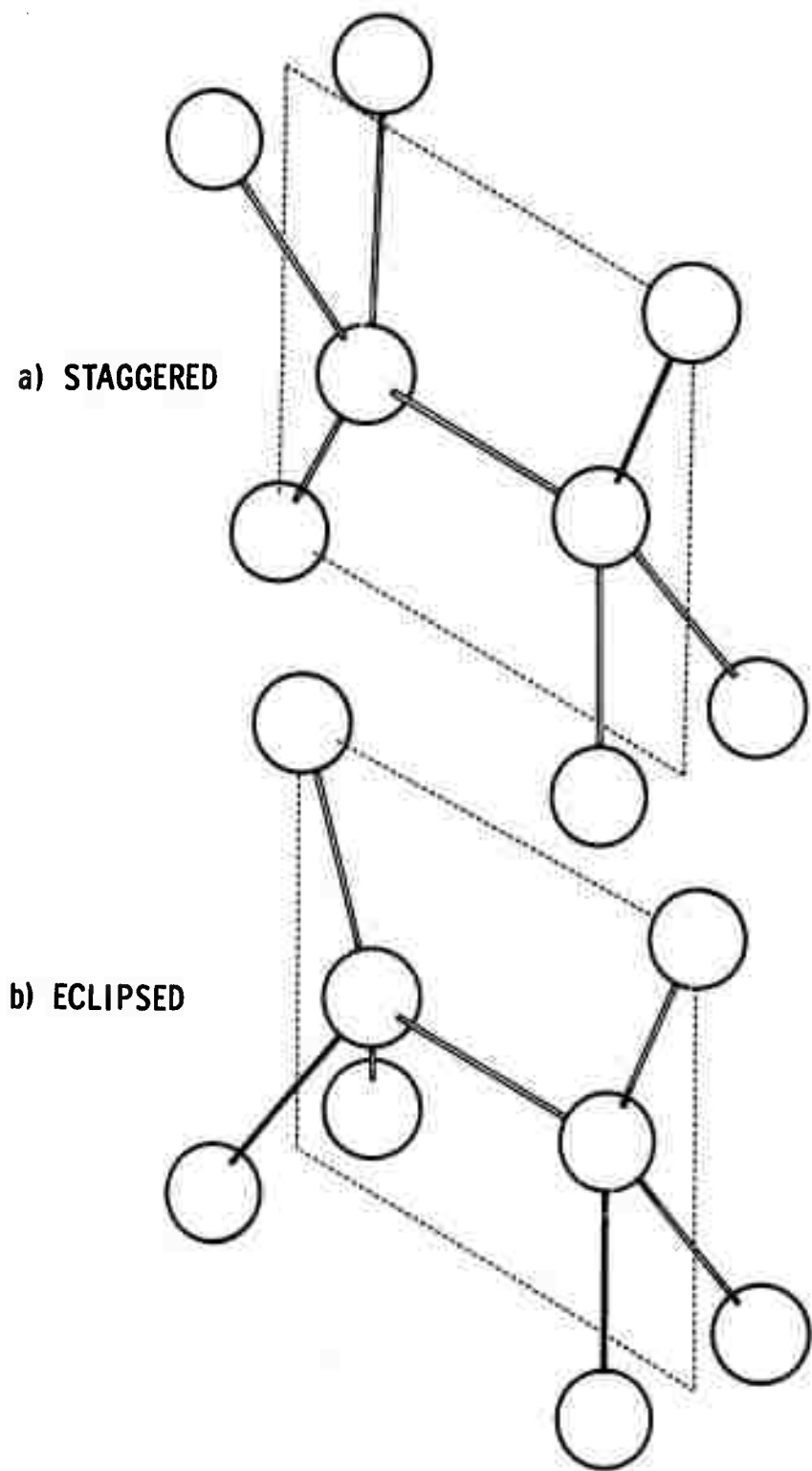


Figure 11

Staggered and eclipsed linking of Ge tetrahedra.

addition to the staggered and eclipsed positions. It is this distribution of orientations about the common bond linking tetrahedra that has a profound effect on the third peak. Polk's model also has a density within 2% of the crystalline density which is consistent with the more recent experimental r.d.f.'s

Amorphous germanium samples were prepared from bulk ingot by resistance heating of a tungsten boat and evaporation onto 1 mil Al foil. The vacuum in the system was about 5×10^{-7} torr before deposition and rose to about 10^{-6} because of radiant heating. The thickness of the foils was approximately one micron; six layers were used to obtain the EXAFS spectra. These samples were studied by x-ray diffraction, electron microscopy and diffraction, and differential scanning calorimetry. The structural investigations showed diffraction patterns with two diffuse rings at $4\pi \sin \theta / \lambda = 1.81$ and 3.22\AA^{-1} . Application of the Scherrer formula to the line width gave an apparent domain size of approximately 40\AA . Microscope investigations revealed a very fine 40\AA wavelet structure on top of a $300\text{-}500\text{\AA}$ "pebble grain" texture. These observations of graininess in amorphous films are consistent with the observations of others and do not mean that the material is microcrystalline³⁹. In the microscope crystallization could be induced with the electron beam and hot stage examination proved a first crystallization step at $150\text{-}200^\circ\text{C}$. This was confirmed with differential scanning calorimetry which showed a slow exothermic reaction beginning about $100\text{-}150^\circ\text{C}$ and continuing until the rapid onset of crystallization about 450°C . These calorimetric observations agree with the earlier work of

Chen and Turnbull⁴⁰. Further work of this nature is being carried out to correlate the structural features observed with EXAFS with features observed with these other techniques.

The crystalline samples consisted of a pure, finely ground powder (59% pure and -325 mesh) which was cast in Duco cement and spread into thin layers on 1 mil Al foil with a glass slide. Several layers were used to give an effective sample thickness of about 6 μ .

The EXAFS data for crystalline and amorphous Ge are shown in fig. 12. The crystalline data is the smoothed curve of fig. 5b. The amorphous Ge is the smoothed curve obtained from 10 data runs. As can be seen in the figure, the crystalline data has considerably more detail than the amorphous curve; however, the major extrema of both curves coincide. The amorphous curve appears to be primarily from a single coordination shell. However, contributions from higher shells can be seen above 600 eV.

The radial structure functions (r.s.f.) of crystalline and amorphous Ge obtained from the Fourier transform of the data are shown in fig. 13. The first peak on both curves has been normalized to unity since only the relative heights of the peaks are compared.

In crystalline Ge the first 6 coordination shells are clearly resolved. The expected positions of the coordination shells are given in Table I in Chapter 2, using a lattice parameter for Ge of 5.65 \AA , while the noted distance in the figure are good to 1% or better. It should be emphasized that EXAFS looks at crystal structure differently from classical crystallography since the

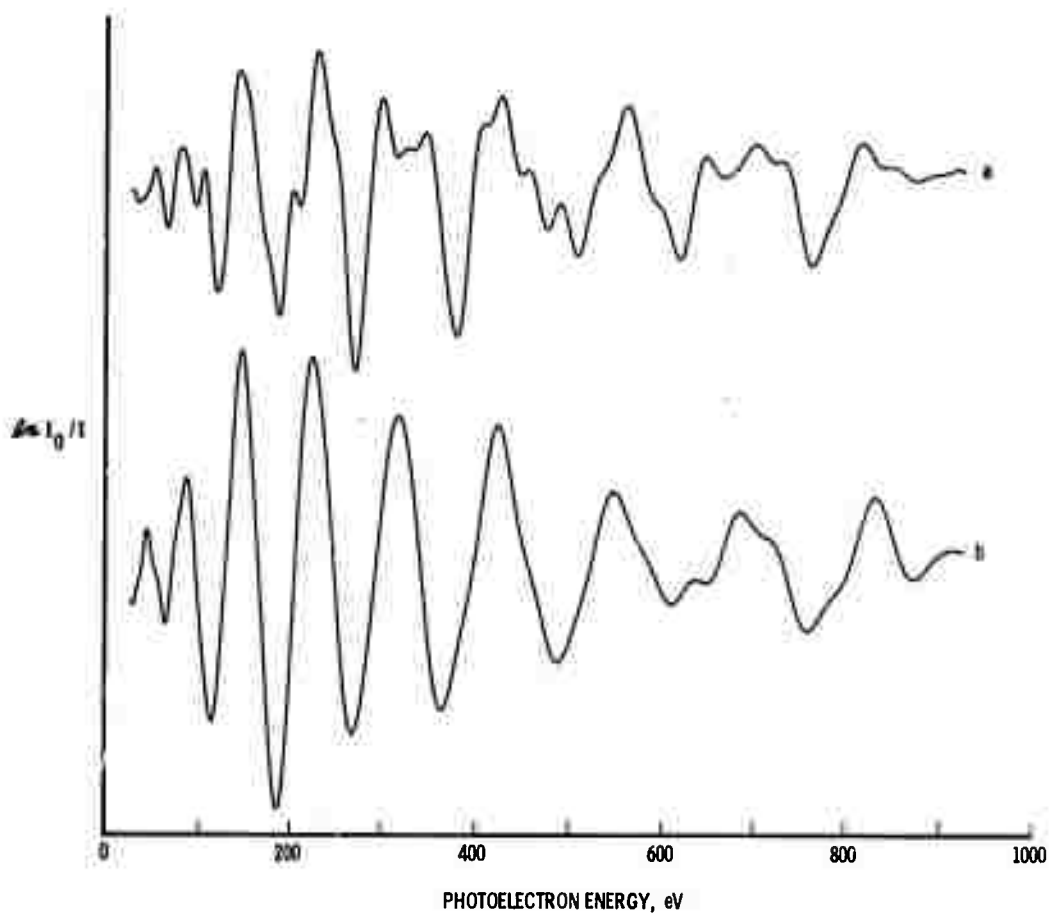


Figure 12

Smoothed experimental EXAFS data for a) crystalline and
b) amorphous Ge.

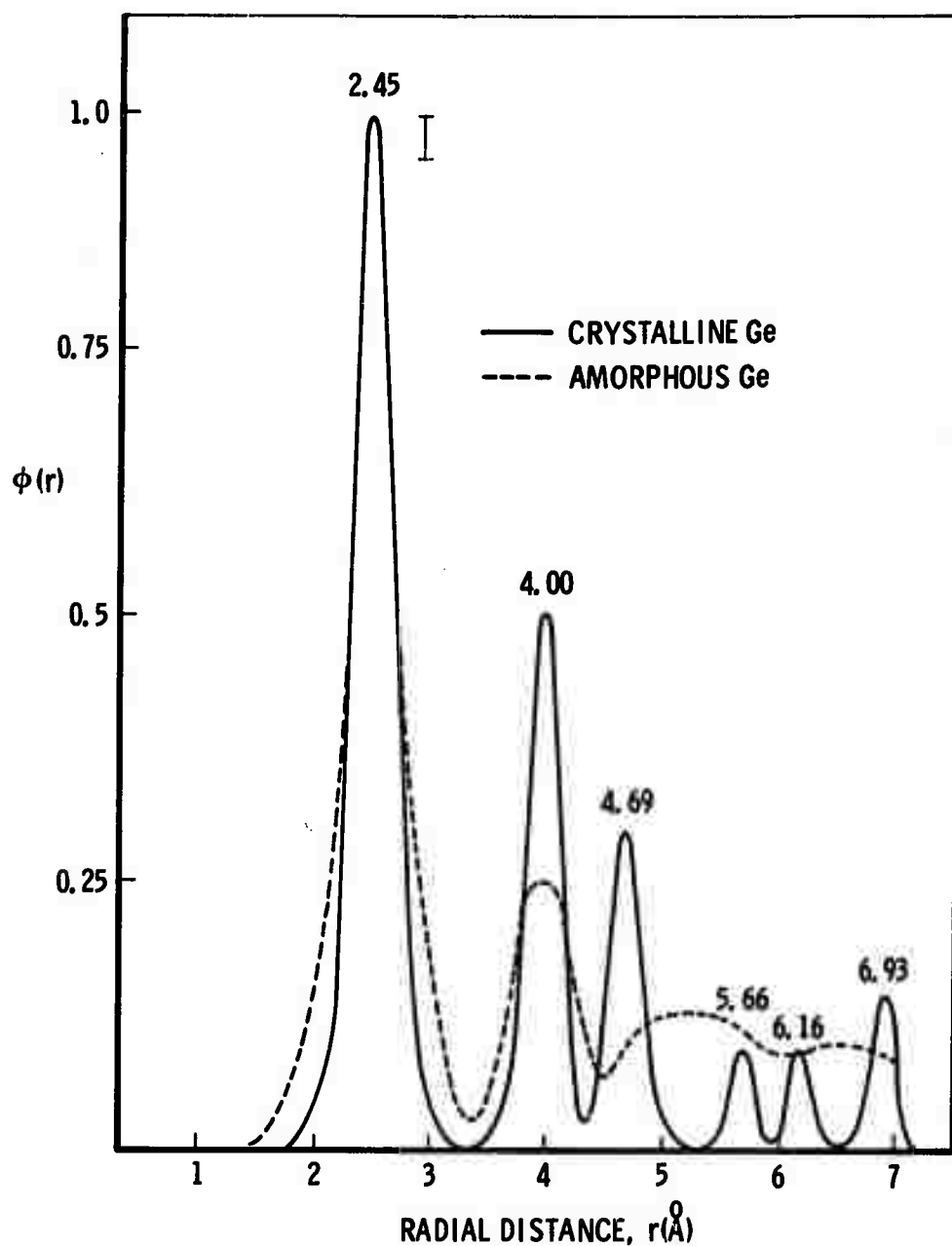


Figure 13

Radial structure functions of crystalline and amorphous Ge obtained from the curves of Fig. 11. The numbers over the peak indicate the measured distance in \AA . The vertical error bar ($\pm 1\sigma$) in Fig. 12, 14, 15, 16 was estimated by replicate analysis.

structure is probed radially with a given type of absorbing atom at the origin. The transform used in obtaining fig. 13 (crystalline Ge) was calculated without the phase shift, so as mentioned in Chapter 3, the peaks were all shifted by $.28\text{\AA}$ to the expected position given in Table II. Note that this shift is in good agreement with the value of $.27\text{\AA}$ obtained from the linear fit of the WKB shift in Chapter 2.

Another parameter that was obtained from the crystalline data is γ . As mentioned in Chapter 3 if N_j , r_j , and σ_j are known then γ may be obtained using the observed A_j 's (noramlized to A_1) and eq. 3-5. The plot obtained from the data is shown in fig. 14. A good straight line is obtained, the slope of which is $\gamma = .31\text{\AA}^{-1}$ which corresponds to a mean free path for scattering into an eigenstate, $1/\gamma = 3.2\text{\AA}$. Because this value is of the order of the interatomic spacing and because the short range structure in crystalline and amorphous Ge is so similar as shown in fig. 13, it is assumed that the same value of γ applies to amorphous Ge. As mentioned previously, this assumption is critical since there is no way to independently determine γ for an amorphous material.

In the amorphous r.s.f. the positions of the first two peaks agree exactly with the crystalline distance while the third peak, is unresolvable above the background.

These results differ from earlier results which found that the interatomic distances were expanded $\sim 3\%$ from the crystalline value⁴¹, and are more in agreement with more recent studies on Ge and Si^{37,38}. This EXAFS technique is not sensitive to macro-

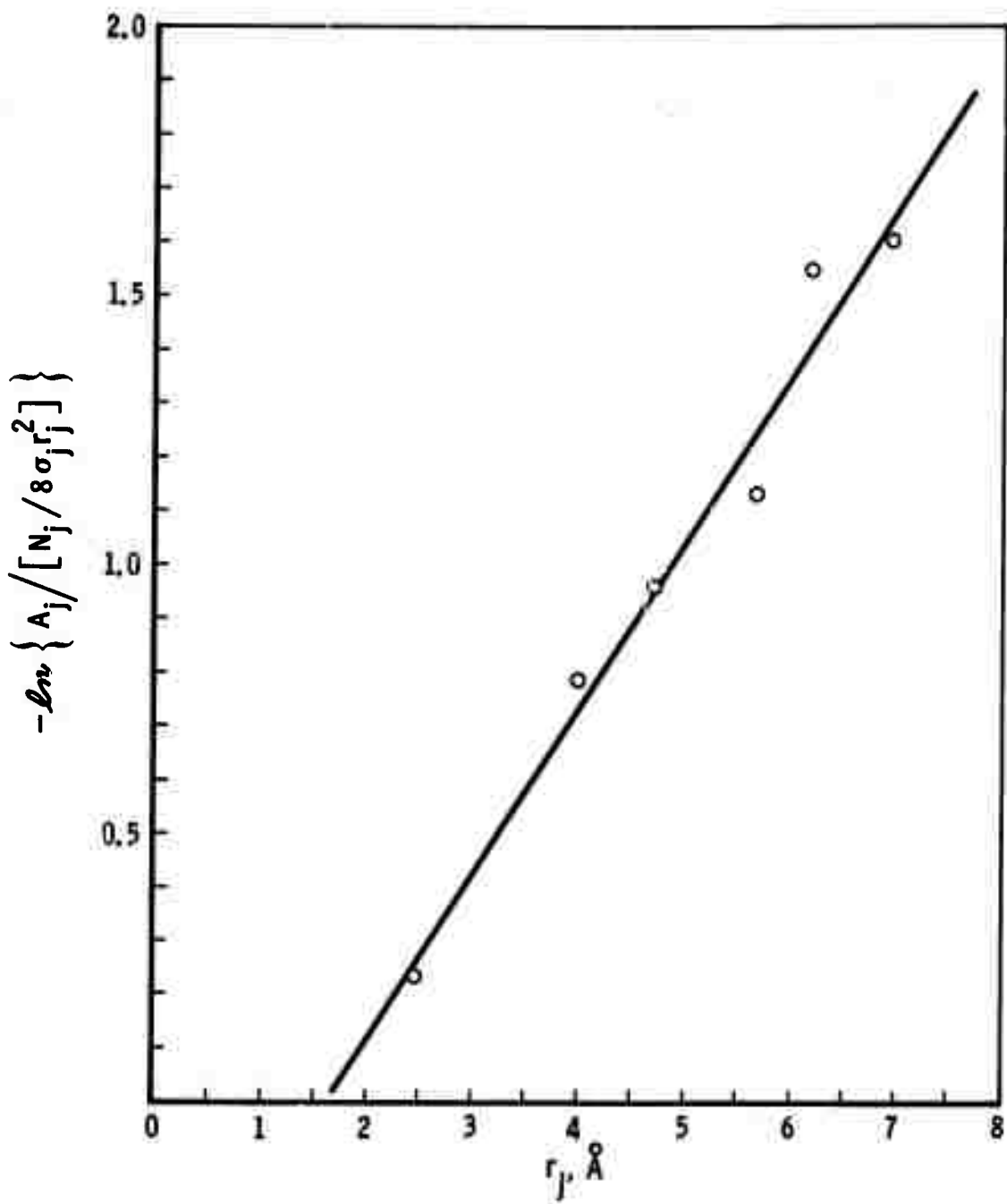


Figure 14

Plot of eq. (3-5) using the measured crystalline Ge amplitudes.

The slope of the curve gives $\gamma = .31$.

or micro-voids; however, a uniform distribution of atomic sized vacancies would contribute to the measured values by causing distortions in the average atomic distances. Micro-voids or larger vacancy clusters were not present since electron diffraction did not show appreciable small angle scattering.

Since the first distance corresponds to the tetrahedral bond distance and the second distance to the edge of the tetrahedron, this result is compatible with a continuous random network of Ge tetrahedra, i.e. the basic tetrahedral unit of crystalline Ge is preserved in amorphous Ge so that the ideal covalent bonding of each Ge atom is satisfied. The tetrahedra are not linked in the regular staggered configuration which leads to the diamond structure, and the bond angle is distorted about its regular tetrahedral value. This destroys the long range crystalline order. This is indicated by the broadened and reduced second peak. The first peak in the crystalline and amorphous curves are very similar in size which is in agreement with the findings of Moss and Gracezyk³⁷ who found that the width of the first amorphous peak in Si was the same as the crystalline width and thermal in origin. If it is assumed that the number of atoms in the second shell and the thermal factor are the same as in crystalline Ge, then by using eq.(3-3) the amplitude difference may be related to a difference in σ_2^D due to disorder broadening. By eq.(3-7) it is found

$$\sigma_2^D(A) \approx 6 \sigma_2^{TOT}(C) \quad (5-1)$$

which gives a disorder smearing of .15 \AA meaning that the tetrahedral bonds are distorted $\pm 5^\circ$.

B. GeO_2

GeO_2 is isostructural with $\alpha\text{-SiO}_2$ and, like Ge, has a basic tetrahedral unit where every Ge is tetrahedrally bonded to 4 oxygens and the oxygen atoms are shared by adjacent tetrahedra. Previous fine structure studies have shown that the EXAFS of amorphous GeO_2 is very similar to the hexagonal or α -quartz form of GeO_2 .^{42,43} This crystal structure is a loose stacking of tetrahedra in a hexagonal unit cell with 3 tetrahedra per unit cell.⁴⁴ The results of earlier studies on the structure of amorphous GeO_2 ^{42,45,46} and SiO_2 ⁴⁷ were consistent with a random network of GeO_2 tetrahedra. Mozzi and Warren⁴⁷ did a thorough study of the radial distribution function of amorphous SiO_2 using pair functions and found good agreement between the data and a continuous random network model of Evans and King.⁴⁸

The crystalline GeO_2 -hex with the α -quartz structure was obtained from Fairmount Chemicals. Absorbers were made by grinding the powder, casting it in Duco cement, and spreading thin layers on 1 mil Al foil. The amorphous GeO_2 -a was made by melting GeO_2 in a quartz tube and quenching into water. The lack of crystallinity was verified by x-ray diffraction which showed only a series of broad, smooth maxima. The amorphous absorbers were prepared in the same fashion as the crystalline GeO_2 , and the thickness of both absorbers was $\sim 10 \mu$.

A comparison of crystalline and amorphous GeO_2 is shown in fig. 15.

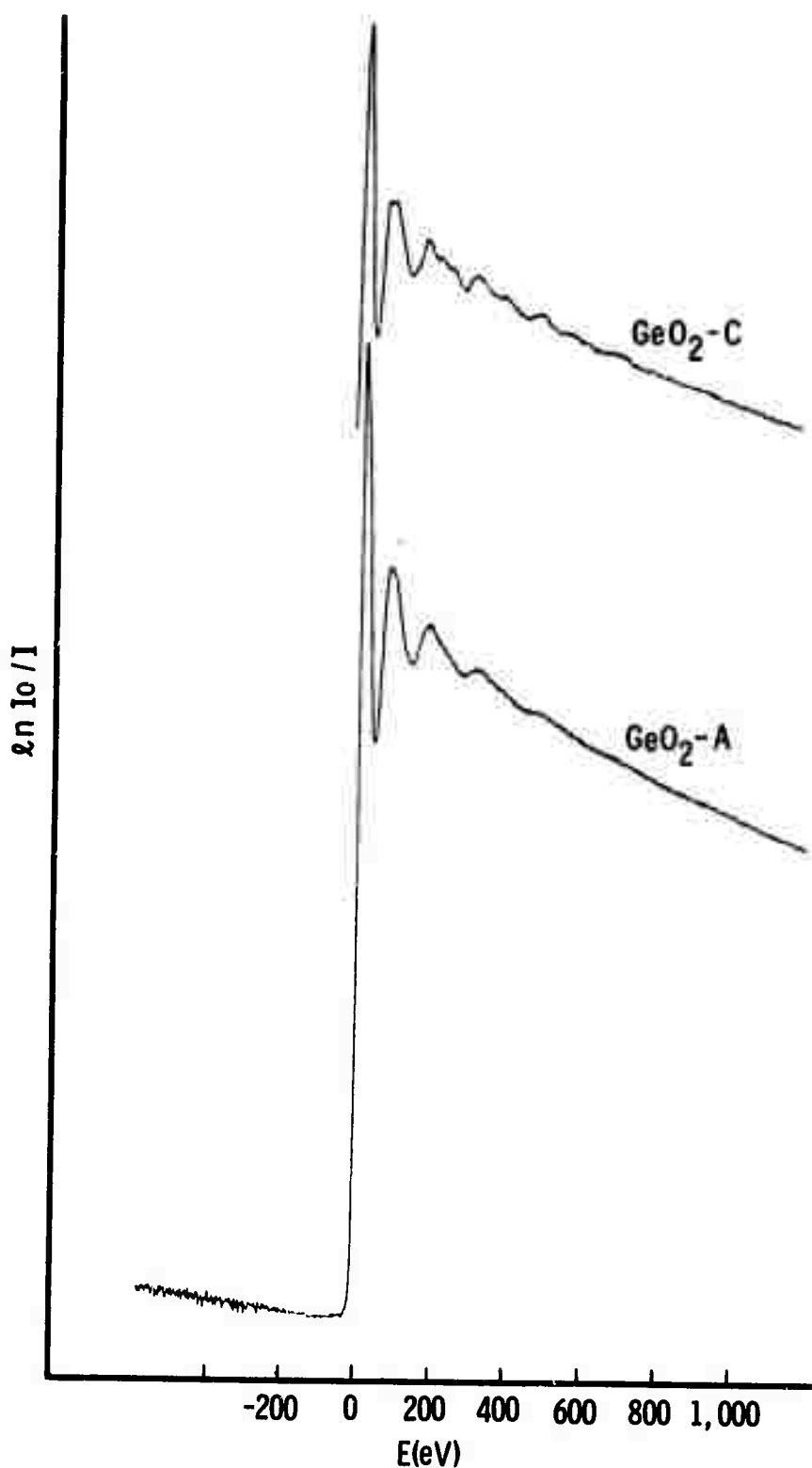


Figure 15

Comparison of crystalline and amorphous GeO_2 EXAFS

The transforms of the experimental EXAFS data is shown in fig. 16. This is data for only the Ge edge since the oxygen edge is beyond current instrumental capability. Both curves have the first peak normalized to unity. When the transforms were taken peaks near $r = 0$ were observed which depended on where the data was terminated near $k = 0$. The data also contained termination ripple of periodicity π/k_m as discussed in Chapter 3. Typically several transforms were done with various ranges of data in order to get transforms which were nearly flat near $r = 0$ and to identify termination ripple. A typical transform curve for GeO_2 -hex is shown in fig. 17 with residual structure and termination ripple left in, and the peaks shifted by "a" from their crystalline distances. The final curves (fig. 16) have had the residual structure near $r = 0$ and termination ripple graphically removed. Work is currently underway to improve the data analysis techniques to eliminate the structure added by the transformation methods. To compare the crystalline data with the expected positions and amplitudes of the peaks from knowledge of the crystal structure, a program was developed which can calculate the number, types, and distances of atoms from a given atom placed at the origin. This program is explained in detail in Appendix B, and the resulting structural information is listed in Table III. The lines in fig. 16 show the expected peak positions and their amplitudes calculated from eq.(3-3). In the expression for the amplitudes shell to shell variations of σ_j were ignored and the difference in scattering factors was accounted for by assuming that each factor was proportional to the number

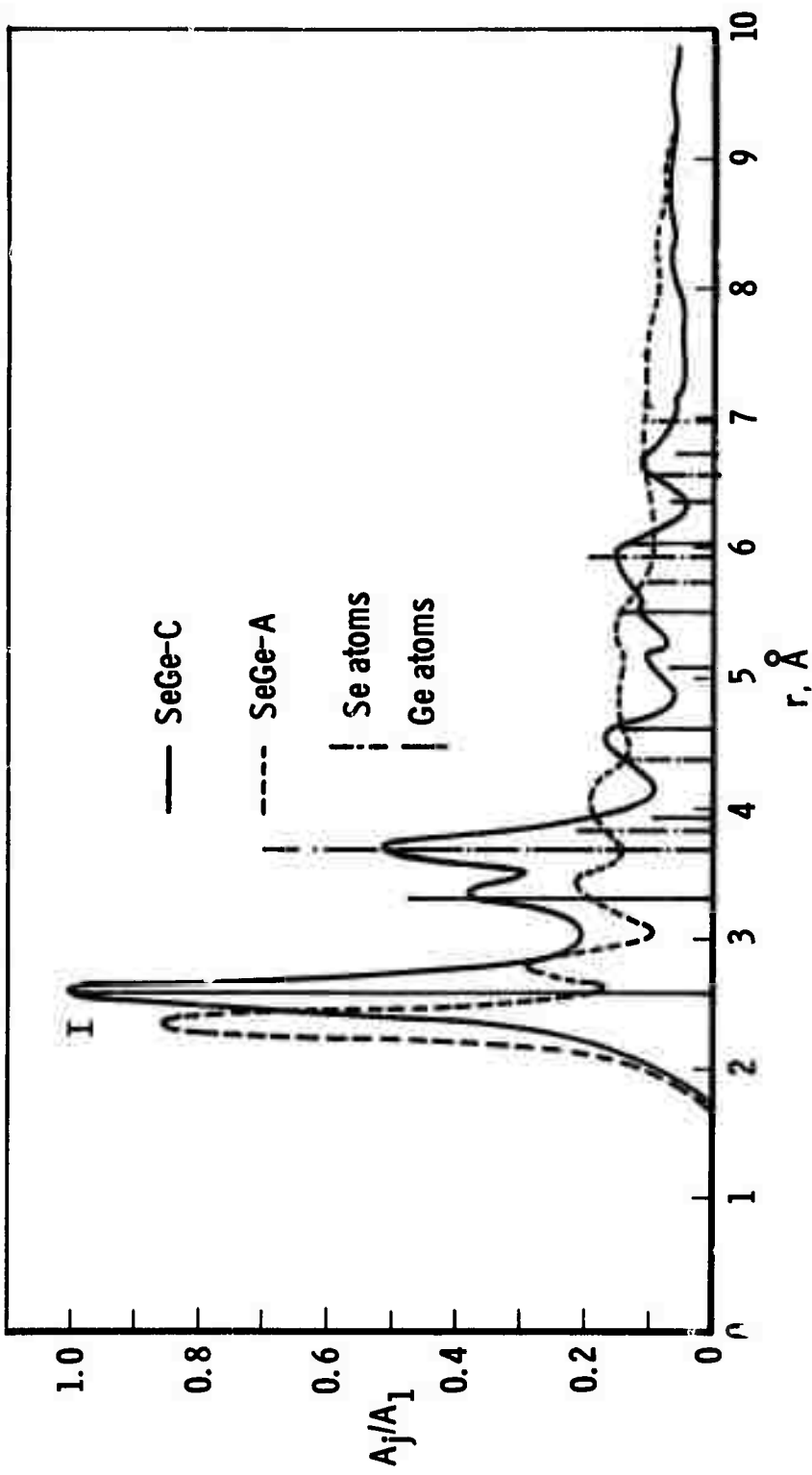


Figure 16

Radial structure functions for crystalline and amorphous GeO_2 . The lines indicate the positions and amplitudes of the crystalline peaks expected from a knowledge of the crystal structure and using eq. (3-3).

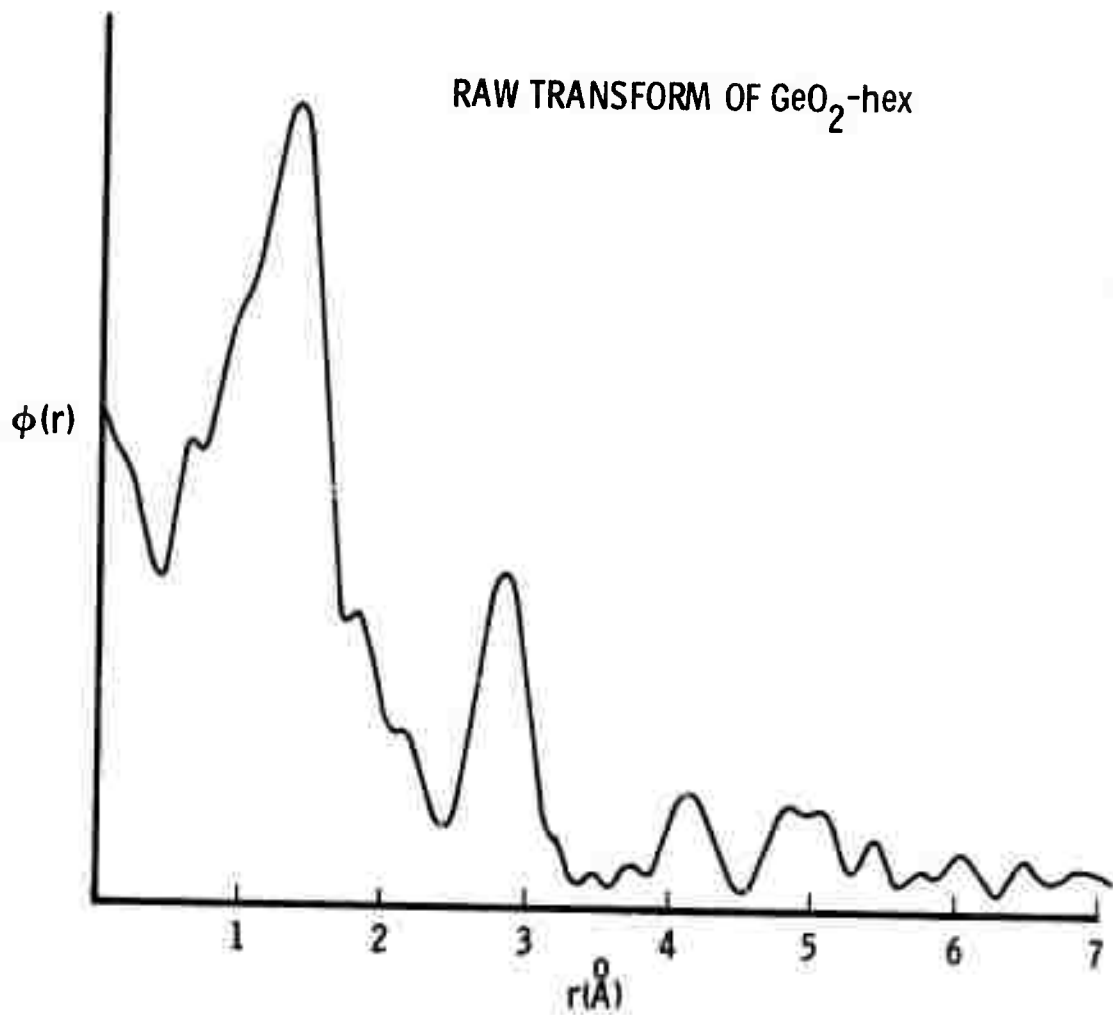


Figure 1.7

Transform of $\text{GeO}_2\text{-hex}$ data showing
termination ripple and structure near $r = 0$.

Table III

EXAFS Structural Data for GeO_2 , GeSe , SeGe

GeO_2			GeSe			SeGe		
N _j	r _j (Å)	atom type	N _j	r _j (Å)	atom type	N _j	r _j (Å)	atom type
2	1.63	0	1	2.56	Se	1	2.56	Ge
2	1.65	0	2	2.59	Se	2	2.59	Ge
4	3.13	Ge	2	3.31	Se	2	3.31	Ge
2	3.56	0	1	3.35	Se	1	3.35	Ge
2	3.62	0	2	3.39	Ge	4	3.68	Se
2	3.70	0	2	3.84	Se	2	3.69	Se
2	4.01	0	4	3.94	Ge	2	3.84	Se
2	4.08	0	4	4.04	Ge	1	3.94	Ge
2	4.17	0	2	4.39	Se	2	4.39	Se
2	4.24	0	2	4.62	Se	2	4.62	Ge
2	4.26	0	1	4.65	Se	1	4.65	Ge
2	4.31	0	2	4.72	Ge	2	5.10	Ge
2	4.42	Ge	2	5.10	Se	3	5.56	Ge
2	4.52	Ge	3	5.51	Se	2	5.51	Ge
2	4.58	0	2	5.54	Se	4	5.74	Se
2	4.64	0	4	5.84	Ge	8	5.84	Se
2	4.68	0	2	6.01	Se	2	6.01	Ge
8	4.97	Ge	2	6.02	Se	2	6.02	Ge
4	5.19	0	2	6.03	Se	2	6.03	Ge
2	5.29	0	4	6.28	Ge	2	6.37	Ge
2	5.49	Ge	2	6.37	Se	2	6.41	Ge
2	5.64	Ge	4	6.41	Se	6	6.58	Se
4	5.74	0	2	6.71	Se	2	6.71	Ge
2	5.95	Ge	2	6.73	Se	2	6.73	Ge
2	5.97	0	5	6.75	1Se/4Ge	1	6.75	Ge
2	5.99	0	4	6.78	Ge	8	6.99	Se
2	6.02	0	2	7.16	Se	2	7.16	Ge
2	6.05	0	2	7.20	Ge	4	7.23	Se
4	6.08	0	2	7.34	Se	2	7.34	Ge
2	6.12	0	2	7.35	Se	2	7.35	Ge

of electrons as shown in Chapter 2, so that $f_{\text{Ge}} = 4f_0$. To obtain a good agreement between the expected crystalline peak positions and the observed peak positions all of the peaks in the r.s.f. had to be shifted by $+.28\text{\AA}$ which is the same phase shift factor found in crystalline Ge.

Comparing the crystalline and amorphous data, the first peak, which is the tetrahedral Ge-O bond, moved in slightly from 1.65\AA to 1.60\AA . The second peak which is the Ge-Ge distance in adjacent tetrahedra decreased from 3.15\AA to 3.07\AA . Although it is possible that some of this difference might be due to differences in the phase shift between GeO_2 -hex and GeO_2 -a, contrary to our assumption of equal phase shifts in the materials; this was not considered as likely as a change in bond length since the k dependence of the Ge phase shifts in crystalline Ge, GeO_2 and GeSe was found to be $.28 \pm .03\text{\AA}$ independent of the crystal structure or whether the bond is covalent or ionic. This means that the Ge-O-Ge bond angle changes from its value of 144° in the crystalline case to $147^\circ \pm 5^\circ$ in the amorphous case. The 25% decrease in peak amplitude can be attributed to a proportionate decrease in the number of atoms or disorder smearing or both. If amorphous GeO_2 is a continuous random network of tetrahedra, then the decrease is more likely due to disorder smearing as in Ge. The third GeO_2 -a peak at 3.85\AA is significantly different from GeO_2 -hex and from the amplitude of the peak it could be due to 1 Ge atom or 4 O atoms if there is no disorder smearing. Since this distance is greater than that possible for a Ge-Ge distance in adjacent oxygen sharing tetra-

hedra, it is tentatively identified with the median oxygen atoms in adjacent tetrahedra and suggests that the alignment of oxygen atoms is more symmetric (like the β -cristobalite structure⁴⁸) in $\text{GeO}_2\text{-a}$ than in $\text{GeO}_2\text{-hex}$. These results suggest that GeO_2 is a continuous random network of tetrahedra which is more ordered than for Ge, and are in general agreement with the earlier studies although these results surpass others in resolution and detail.

C. GeSe

The final system studies was GeSe which was chosen to illustrate the power of the EXAFS technique to probe the structure around individual atomic species. The crystal structure of GeSe is highly distorted NaCl structure of the SnS type^{50,51} with each atom having 6 neighbors of the opposite kind (3 at $\sim 2.58\text{\AA}$ and 3 at $\sim 3.33\text{\AA}$). However, beyond the second neighbors the structure about a Ge atom and a Se atom differ. Unlike Ge and GeO_2 , there is no easily identifiable basic structural unit in either the crystalline or amorphous case.

Crystalline GeSe was prepared by heating equiatomic portions of pure Ge and Se in a solid quartz tube for several hours at 900°C and quenching in water. The crystal structure was verified from the x-ray diffraction pattern which agreed with the listed pattern in the ASTM files. Absorbers were prepared by grinding the GeSe into a fine powder and mixing it with Duco cement and spreading thin layers onto Al foil. Amorphous samples were prepared by vacuum evaporation under the same conditions as

amorphous Ge. The problem of non-stoichiometric sublimation of GeSe was recognized⁵², and since a multiple furnace technique was not available, various sized pieces of GeSe were sublimed simultaneously in order to get a uniform deposition. Measurements of the relative x-ray absorption coefficients proved that the resultant films were within 3% of the composition of the initial evaporants although this does not prove that the material is homogeneous. Some differential scanning calorimetry was done which showed a single exothermic crystallization peak at about 350°C which indicated that the material is homogeneous and not phase separated Ge or Se, which crystallize at 450°C and 70°C respectively. The thickness of both the crystalline and amorphous GeSe absorbers was ~10μ.

The K edge absorption fine structure for both the Ge and Se atoms in amorphous GeSe was shown in fig. 1 and a comparison of the crystalline and amorphous EXAFS for both edges is shown in fig. 18. The differences in the EXAFS can be seen although a close inspection would show that the basic periodicity of the major extrema is the same. The radial structure functions of both crystalline and amorphous GeSe is shown in fig. 19 a and b. Note that the r.s.f.'s are relative to a Ge and an Se atom, respectively. As in fig. 16 the lines indicate the positions of the atoms in the crystal relative to either a Ge or Se atom calculated from the computer program of Appendix C with the amplitudes from eq. 3-3 ignoring possible differences in the σ_j 's. The crystalline data shows that the experimental r.s.f.'s from each edge agree quite well with the predicted structure and that the

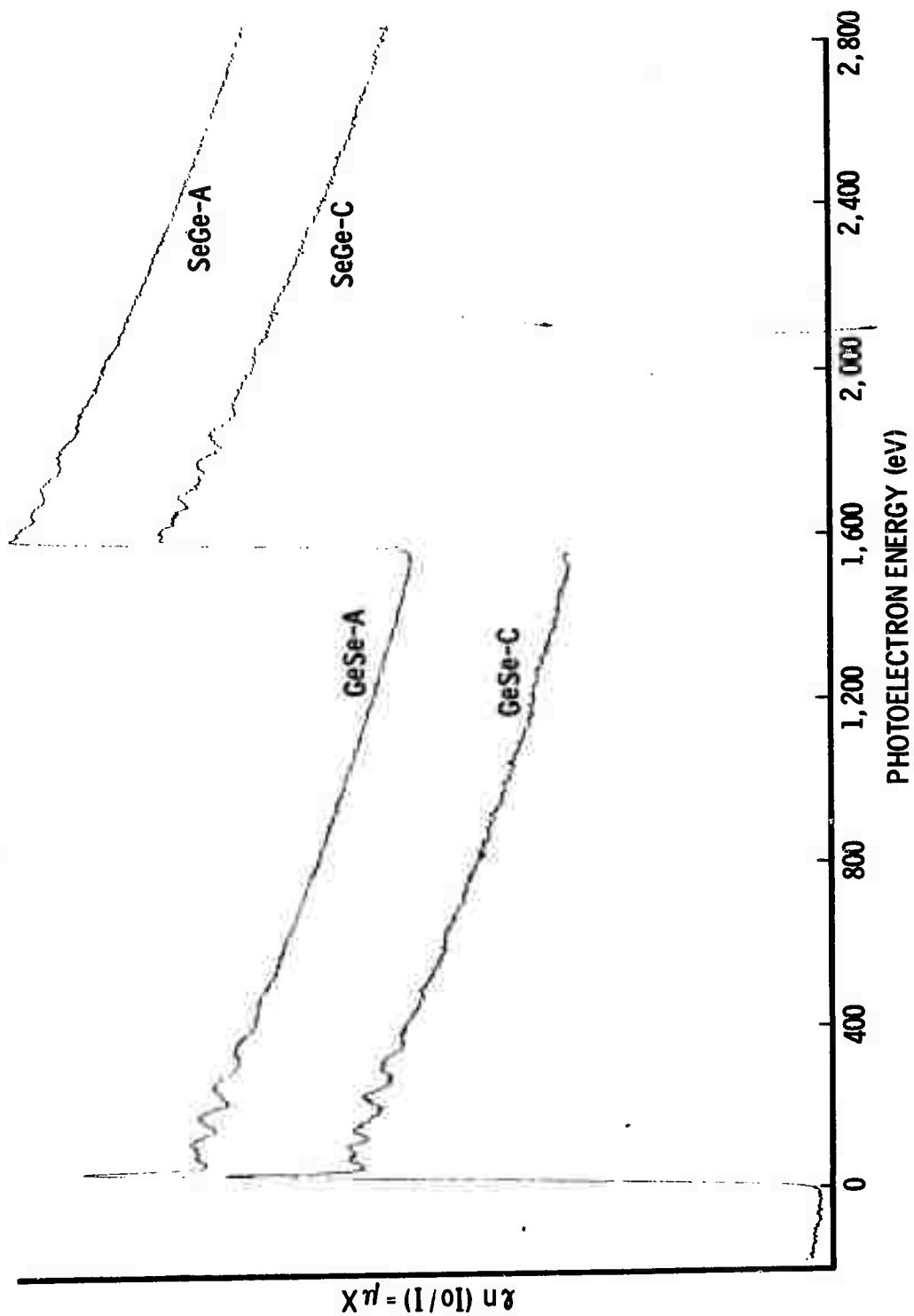


Figure 18

Comparison of crystalline and amorphous
GeSe EXAFS for both Ge and Se edges.

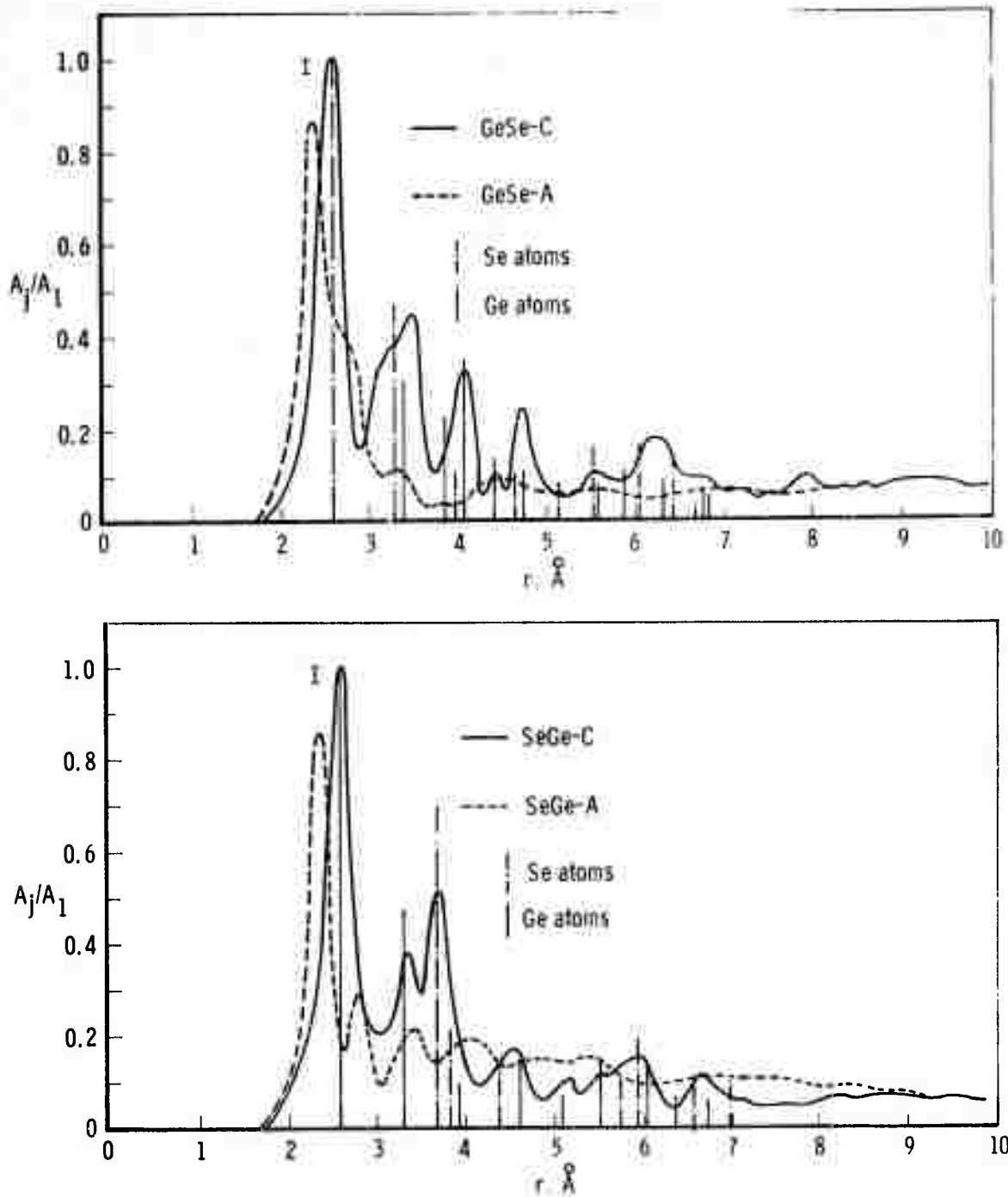


Figure 19

Radial structure functions for crystalline and amorphous GeSe with respect to a Ge atom (19a) and an Se atom (19b) at the origin. The lines indicate the positions and amplitudes of the crystalline peaks expected about each kind of atom from a knowledge of the crystal structure and eq. (3-3).

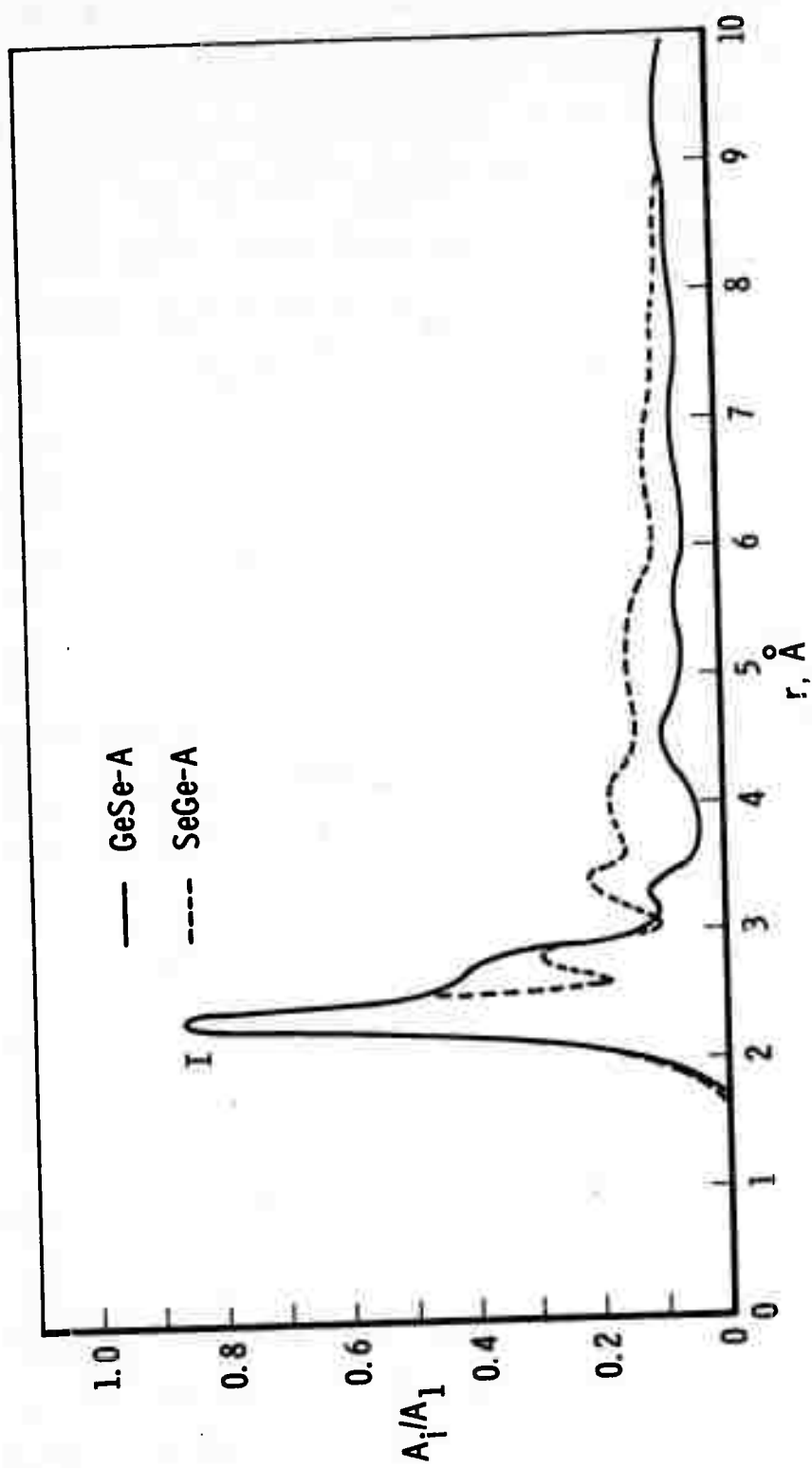


Figure 20

Comparison of the rsf's about the
Ge and Se atom in amorphous GeSe.

at 2.35\AA which gives 1 atom at 2.80\AA using eq. 3-3. Since the ideal GeSe covalent bond is 2.37\AA , it appears that in going from the crystalline to the amorphous material the material has changed from a more to a less distorted covalent bonding arrangement for the nearest neighbor.

In fig. 20 the splitting around the Se atom is more clearly resolved and may illustrate the tendency of Se to link two nearby Ge atoms into a chain as the other nearby Ge atom is forced away. The less resolved splitting about the Ge atom may be due to bonding to another Ge atom (perhaps at the Ge-Ge bond distance of 2.45\AA) which would indicate the tendency of Ge to form tetrahedrally directed bonds. A satisfactory structural unit incorporating these features and satisfying all bonding requirements has not yet been visualized.

Chapter 6

Discussion and Conclusions

Although EXAFS has been shown to arise from a complex interaction of the ejected photoelectron with the surrounding atoms, it is measured by simply determining the probability of an x-ray photon being absorbed at a given energy. This probability is related to the overlap of the initial K electron wave function with the final ejected photoelectron wave function. If the final photoelectron wave function contains significant scattering contribution from atoms nearby to the absorbing atom, then oscillations in the absorption coefficient as a function of energy will appear. Thus, oscillations in the absorption probability (which are measured as variations in I/I_0 as a function of energy) are determined by the location of the surrounding atoms. This interaction is "sensed" by the x-ray photoelectron during the time of its interaction with the K shell electron. The quantum mechanical calculation is straight forward once the physical mechanism is understood. Treatment of the surrounding atoms as a system of weak point scatterers simplifies the calculation of the scattered waves yet retains the physics of the problem. The final result (eq. 2-33) contains the energy dependence of the scattering, a temperature factor, and a range term which allows calculation of spectra in quantitative agreement with the observed EXAFS for three different crystal structures. Eq. 2-33 is sufficiently general that it can be applied to any system where EXAFS is observed (crystalline and non-crystalline solids, liquids, and polyatomic gases) and for either unpolarized or polarized x-rays.

For unpolarized x-rays ($e_x^2 = e_y^2 = e_z^2$) or for materials with cubic symmetry ($x_i^2 = y_i^2 = z_i^2$), the result simplifies to eq. 2-34.

However, this result may also be used to explain the orientation dependence of EXAFS observed with polarized x-rays and single crystals of non-cubic materials in a more direct way than has been done previously.⁵² Future work is planned to use the point scattering model to calculate the L_{II} and L_{III} spectra which are dominated by the 2p electrons making transitions to d symmetric states in the continuum. These calculations are complicated by a more complex angular dependence for both the initial and final electron wave function.

The most important result of the point scattering theory shows that EXAFS can be Fourier transformed to give a radial structure function for each kind of atom in a material. The r.s.f. contains information on the number and kinds of atoms and their distribution about the coordination distances. The r.s.f. is superior to the radial distribution function in several ways. The main advantage is the radial distribution function only calculates a two-body correlation function, whereas the r.s.f. determines the average structure about each different kind of atom in a multicomponent system. This information (note the GeSe data) can be essential for understanding the structure. Another advantage is that the r.s.f. has potentially twice the resolving power of the r.d.f. since there are twice as many oscillations in the EXAFS data over the same range of k space. And, finally, the

natural definition of the r.s.f. as a sum of Gaussian curves from each coordination shell allows the height and width parameters to be measured for each shell, while the r.d.f. [defined as $4\pi r^2 \rho(r)$] determines the positions of the atomic shells as fluctuations about the average (parabolic) density curve. Fitting Gaussian curves to determine the area of the r.d.f. peaks is usually only possible for the first peak and even then may be ambiguous because of contributions from different kinds of atoms in a multicomponent system.

Many of the disadvantages of the EXAFS technique can be overcome by further developments. These include improvements in data analysis to lessen termination effects in the data, development of a theory for the L_{II} and L_{III} edges to obtain structural information from those materials where the K shell is too high in energy, acquisition of a vacuum double crystal x-ray spectrometer to extend the range of material whose K or L edges may be measured (this includes the whole periodic table), and improved data acquisition techniques to speed up and simplify the data gathering and analysis.

There remain some inherent disadvantages of the EXAFS method: The amorphous data must be compared to the crystalline data in order to account for parameters such as ϵ_T , γ , n , and the amplitude normalization for the material. A more serious limitation is that in multicomponent samples the relative absorption of each element whose EXAFS is to be studies must be large enough so that the fine structure can be resolved. (e.g.--a few atomic % of a light element in a heavy element matrix could not be measured.) This is the main experimental limitation, but it still leaves a

wide range of systems which can be studied.

Some tentative conclusions on amorphous structures can be drawn from the three systems studied here. Two of the systems (Ge and GeO_2) were examples of a continuous network of tetrahedra. In both cases the tetrahedral unit which is the basis of the crystal structure is preserved in the amorphous system. In Ge each atom forms an ideal covalent bond with 4 neighbors at a distance of 2.45\AA , while in GeO_2 each Ge has 4 tetrahedrally bonded oxygens with each oxygen acting as a bridge between tetrahedra by bonding with two Ge . The Ge-O bond is partially ionic with a length of 1.60\AA . The networks built up from these tetrahedra are substantially different. In Ge adjacent tetrahedra are oriented randomly about the common Ge-Ge bond which leads to a very rapid reduction in order beyond the second distance. The GeO_2 network differs from Ge since the oxygen atoms must be shared by adjacent tetrahedra, so that the order in this system extends out beyond the neighboring tetrahedra. In GeSe the situation is much different. The crystalline state is a highly distorted NaCl structure with each atom having 3 neighbors of the opposite kind at $\sim 2.58\text{\AA}$ and 3 neighbors of the opposite kind at 3.33\AA . These bonds are highly distorted from the ideal covalent or ionic bond. In the amorphous material the structure changes so that 2 of the atoms move into a distance of 2.35\AA (which is the GeSe covalent bond length), while the other near-neighbor atom moves out to 2.80\AA . Around the Ge atom there is also evidence of a 4th atom at 2.45\AA (the Ge-Ge distance). All

of these results show that each atom tries to satisfy its ideal bonding conditions in the amorphous state (i.e. 2 atoms in a chain in Se, and 4 tetrahedrally bonded neighbors in Ge). We make the following general postulate for amorphous structures: In covalently or ionically bonded amorphous systems when the requirements of long range order are removed, the near neighbor structure is determined when each atom achieves its ideal bonding state to the extent possible considering the composition of the material. This postulate supports the earlier models of satisfaction of each atom's covalent bonding requirement in amorphous semiconductors by Mott⁵⁴ and Cohen, Fritzsche, and Ovshinsky.⁵⁵ Further work is planned on certain compositions in the Ge-As-Se system to verify this statement.

In summary, the main conclusion of this work is that K edge EXAFS is given by

$$x(k) = -kf(k) \sum_j \frac{N_j e^{-\gamma r_j}}{r_j^4} e^{-2\sigma_j^2 k^2} \sin(2kr + 2\eta(k)) \quad (6-1)$$

$$x(e_x^2 x_i^2 + e_y^2 y_i^2 + e_z^2 z_i^2)$$

which not only allows calculation of fine structure spectra which are in good agreement with observed spectra for any x-ray polarization system where the structure is known, but whose Fourier transform allows structure determination in systems where the structure is unknown. Application to several systems has clearly

demonstrated that it is a powerful technique with some unique capabilities with respect to the standard scattering techniques. The EXAFS technique shows promise of becoming the primary method for structure determination in amorphous materials.

Appendix A

Filtering Methods

The absorption spectrum obtained from the x-ray data contains three components: (1) the K absorption edge followed by a monotonically decreasing absorption coefficient above the edge; (2) the EXAFS added to this above the edge, and (3) the random statistical counting noise superimposed on all of the data. The EXAFS must be separated from the other two components. This could be done by fitting some functional form to the usual photoelectric spectrum, subtracting it from the data, and then using a running average of data points to reduce the effect of the noise. The major difficulty is that the functional form of each edge is not well known and would require an extensive fitting effort for each absorption edge.

The approach used here entails filtering in the large in which the data is Fourier transformed and the frequency components of the desired signal are extracted from the whole spectrum by filtering out the undesired components and then retransforming the filtered data. This method is particularly suited for the EXAFS technique since the first component contains only very low frequency components, the EXAFS signal (component 2) is limited to a small band of frequencies, separated from the low frequency end, while the random noise (component 3) has contributions over the entire domain. The photoelectric background is removed by first subtracting the lowest frequency components from the transformed data.

Although some small contribution from higher frequencies may still exist in the data, close inspection of the EXAFS obtained using this method showed no residual effects of the background.

Since the EXAFS components are limited to the middle range of the total domain, the noise is removed by filtering out all higher components. This is shown in fig. 21 where the arrows indicate the high and low cuts. Although the smoothed EXAFS contains a small contribution from the components of the noise within the same band as the signal, this is only important at the upper end of the spectrum as can be seen in fig. 5b. When the transformation techniques of Chapter 3 are applied to the data the noise is left in to assure that all of the signal is also included.

The actual computer algorithm used to transform the data is the HARM program from the IBM Scientific Subroutine Package which is based on the Fast Fourier Transform method originally developed by Cooley and Tukey.⁵⁶ This program requires that the data be taken in equally spaced intervals in one domain and that the number of points be a power of 2 (usually $2^{10} = 1024$ points; zeros can be appended to get the proper number of points). The data is Fourier analyzed in terms of the real and imaginary components of 512 frequencies. The lowest frequency has a wavelength of twice the range of the data and the remaining frequencies are the next 511 harmonics of this fundamental. The filtering is then done in terms of this finite set of frequencies.

The actual data is taken in equal steps in angle (2θ). The FFT filtering to remove the photoelectron background is done with this data. However, during the transformation to obtain structural

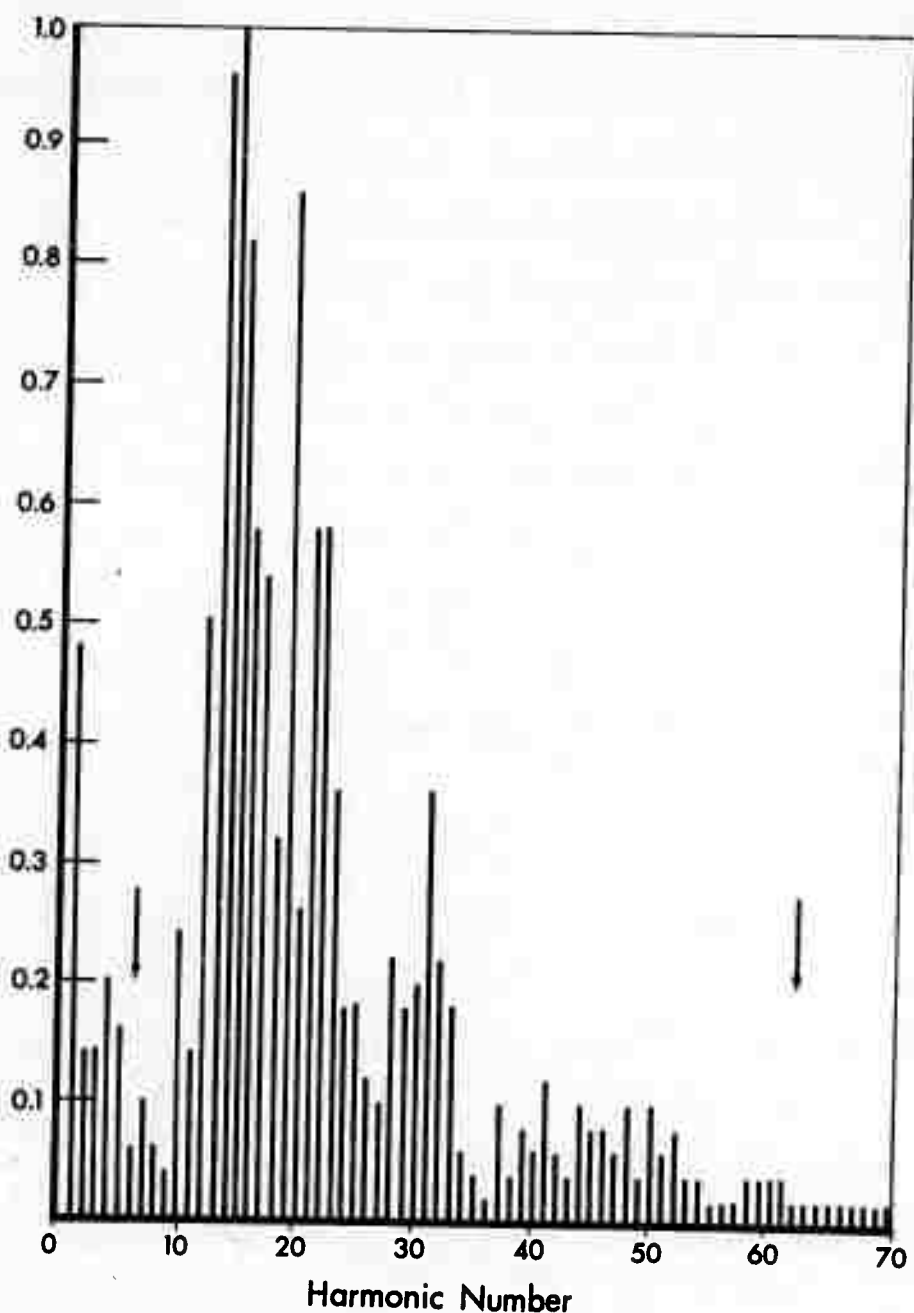


Figure 21

Example of a frequency spectrum of the raw data using the fast Fourier transform. The arrows show the high and low frequency cutoffs. Only 70 of the 512 components are shown; all higher components are negligible.

information, an interpolation routine is used to generate a set of data which is equally spaced in k and then Fourier transformed, as in Chapter 3, to obtain the radial structure function.

Appendix B

Atomic Structures for EXAFS

In the point-scattering theory of EXAFS the positions of the atoms are located by the ejected photoelectron as it propagates radially outward from the absorbing atom. In crystalline materials the surrounding atoms are located from a given atom at a discrete series of distances known as coordination shells. This is a different way of looking at crystal structure than in classical crystallography which gives the structure in terms of a unit cell which may or may not have a particular atom at the origin, and, in fact, the crystal structure in terms of coordination shells is only listed for a few of the simplest crystal structures (simple cubic, fcc, bcc, dia cubic, hcp).

To calculate EXAFS from eq. 2-34 for a known crystal structure or to determine the location and amplitudes of the peaks in a crystalline r.s.f. using eq. 3-3, a general computer program was developed which can compute the structure in terms of coordination shells about a given atom if the unit cell is known. This program will work for any symmetry, and for any number of atoms in the unit cell and is limited only by the core size of the computer used. The input required is (1) the lengths and angles between the coordinate axes in the unit cell ($a, b, c; \alpha, \beta, \gamma$ in the usual crystallographic notation), (2) the number of kinds of atoms, (3) the number of atoms of each kind in the unit cell, (4) the maximum number of lattice translations along each coordinate axes, and (5) if there is no atom at the origin, the displacement needed to bring

a particular atom (corresponding to the absorbing atom) to the origin. Because the program tallies each atomic position, including the positions of the translations of the unit cell, core limitations permit only those atom positions in a volume within about 10 near neighbor distances in each direction to be determined. This is not a severe restriction since EXAFS only probes about 10 Å from the absorbing atom, so that in atoms with large unit cells (e.g. with 72 atoms in a unit cell) only one or two translations in each direction are needed to find all of the distances of interest for EXAFS.

The computer program calculates the x, y, and z coordinates for all of the atoms of a given type relative to a particular atom at the origin using a nest of DO loops. The distances of the atoms from the origin are then computed using the general formula

$$r = (x^2 + y^2 + z^2 + 2xy \cos \gamma + 2yz \cos \alpha + 2xz \cos \beta) \quad (B-1)$$

where α , β , and γ are the angles between the coordinate axes. The program prints out the type of atom, which atom of that type it was, the translations made along each coordinate axes and the total distance (using eq. B-1), and a histogram showing the distances and number of atoms at the distance. If the compound of interest has two types of atoms (say A and B with A being the absorbing atom), the program first calculates the A-A distances and histogram, then the A-B distances and histogram, and finally a total histogram. The same thing could then be done for the B atoms by moving a B atom to the origin of the coordinate system.

This program is also useful in materials where there may be several non-equivalent positions for a given type of atom. The structure for each separate position can be found by moving each different position to the origin. The structure used to calculate EXAFS is then the average structure from the different positions of the same atom since the EXAFS just reflects the average structure about a particular kind of atom.

Typical data from this program has been shown in Table III and a listing of the program is given in Appendix C.

Appendix C

Computer Program Listings

A EXAFS Atomic Structure Program

```
C EXAFS STRUCTURE PROGRAM USING EQ (B-1)
C
REAL DAZ(3,10),RHO(2,4,9,9,9)
REAL UX(3,24),UY(3,24), UZ(3,24),DAX(3,24),DAY(3,24)
DIMENSION NOPOCK(1001),NOTOTP(1001),N(5)
DATA IASTER/1H*/
DATA IBLANK /1H /
MAXSUB=501
MAXSUB=901
C
C READ INPUT DATA
C
READ(5,901) A,B,C,AL,BE,GA
READ(5,902) MH,MK,ML,NAS,N(1),N(2)
NA=N(1)NB=N(2)
C
C READ ATOMIC COORDINATES
C
DO 100 J=1,NA
READ(5,904) UX(1,J),UY(1,J),UZ(1,J)
WRITE(6,101) NA,NB,NAS,UX(1,J),UY(1,J),UZ(1,J)
101 FORMAT(3I5,3F10.4)
100 CONTINUE
IF(NB.EQ.0) GO TO 200
DO 200 K=1,NB
READ(5,904) UX(2,K),UY(2,K),UZ(2,K)
200 CONTINUE
RAD= 3.1415926/180.
ALPHA=AL*RAD
BETA=BE*RAD
GAMMA=GA*RAD
MAH=2*MH+1
MAK=2*MK+1
MAL=2*ML+1
C
C INITIALIZE HISTOGRAM
C
DO 205 I=1,MAXSUB
NOTOTP(I)=0
205 CONTINUE
DO 1 I=1,NAS
NA=N(I)
WRITE(6,902)NAS,NA
DO 210 IPOCK=1,MAXSUB
NOPOCK(IPOCK)=0
```

```

210 CONTINUE
      WRITE(6,905)
C
C      FORM X COORDINATES FOR ALL ATOMS
C
      DO 2 IH=1,MAH
      X=IH-MH-1
      IX=X
      DO 10 JA=1,NA
10    DAX(I,JA)=(X+UX(I,JA))*A
C
C      FORM Y COORDINATES FOR ALL ATOMS
C
      DO 3 IK=1,MAK
      Y=IK-MK-1
      IY=Y
      DO 20 JB=1,NA
20    DAY(I,JB)=(Y+UY(I,JB))*B
C
C      FORM Z COORDINATES FOR ALL ATOMS
C
      DO 4 IL=1,MAL
      Z=IL-ML-1
      IZ=Z
      DO 30 JC=1,NA
      DAZ(I,JC)=(Z+UZ(L,JC))*C
      DX=DAX(I,JC)
      DY=DAY(I,JC)
      DZ=DAZ(I,JC)
C
C      TRANSLATE COORDINATES SO THAT A PARTICULAR ATOM IS AT THE ORIGIN
C
      DX=DX-.226*A
      DY=DY-.226*B
      DZ=DZ-.226*C
C
C      GENERATE DISTANCES USING EQ (B-1)
C
      RHO(I,JC,IH,IK,IL)=SQRT(DX*DX+DY*DY+DZ*DZ+2.*DX*DY*COS(GAMMA)
1 +2.*DY*DZ*COS(ALPHA)+2.*DX*DZ*COS(BETA))
      DIST=RHO(I,JC,IH,IK,IL)
      NSUB=IFIX(DIST*100.)+1
      MARK=IASTER
      IF(NSUB.GT.0 .AND. NSUB.LE.MAXSUB)GO TO 220
      MARK=IBLANK
      GO TO 222
220  NOPOCK(NSUB)=NOPOCK(NSUB)+1
      NOTOTP(NSUB)=NOTOTP(NSUB)+1
C
C      WRITE OUTPUT
C
      222 WRITE(6,906)I,IX,IY,IZ,JC,DIST,MARK
      30 CONTINUE
      "CONTINUE"

```

```

C
C   GENERATE THE HISTOGRAMS
C
C   WRITE(6,908)
908 FORMAT(1H1)
      DO 230 IHIST=1,MAXSUB
      BOT=FLOAT(IHIST-1)*.01
      TOP=FLOAT(IHIST)*.01
      NPHIST=NOPOCK(IHIST)
      IF(NPHIST .LE. 110 )GO TO 225
      WRITE(6,810)BOT,TOP,I
      GO TO 230
225 CONTINUE
      IF(NPHIST.GT.0)WRITE(6,809)BOT,TOP,NPHIST,I,(IASTER,IAST=1,
     1NPHIST)
809 FORMAT(1X,F5.2,F7.2,15,2X,1I1,110A1)
810 FORMAT(1X,F5.2,F7.2,7X,I1,' TOO LARGE TO HISTOGRAM')
230 CONTINUE
1 CONTINUE
      IF(NAS.LT. 2)STOP
      WRITE(6,908)
      DO 330 IHIST=1,MAXSUB
      BOT=FLOAT(IHIST-1)*.01
      TOP=FLOAT(IHIST)*.01
      NPHIST=NOTOTP(IHIST)
      IF(NPHIST .LE. 110)GO TO 325
      WRITE(6,910) BOT, TOP
      GO TO 330
325 CONTINUE
      IF(NPHIST.GT.0)WRITE(6,909)BOT,TOP,NPHIST,(IASTER,IAST=1,
     1NPHIST)
909 FORMAT(1X,F5.2,F7.2,15,2X,1H1,110A1)
910 FORMAT(1X,F5.2,F7.2,7X,'I TOO LARGE TO HISTOGRAM')
330 CONTINUE
      STOP
901 FORMAT(6F12.5)
902 FORMAT(6I3)
904 FORMAT(3F10.4)
905 FORMAT(1H1,4X,1HI,5X,1HH,5X,1HK,5X,1HL,5X,1HN,7X,4HDIST)
906 FORMAT(5(1X,15),2X,F10.4,1X,A1)
      END

```

B Theoretical EXAFS Program

C
C THEORETICAL EXAFS PROGRAM USING EQ(2-34)
C
REAL K,K1
REAL C(4)
DIMENSION CHI2(501,30)
DIMENSION ETA(501),CHI1(501),E(501),K(501)
DIMENSION AN(30),D(30),Phi(30),RHO(30)
DIMENSION AF(4),BF(4)
DIMENSION HOL(20)
PI=3.14159265
CMIN=1.E70
CMAX=1.E70
C
C LATTICE PARAMETER FOR COPPER
C
A=3.61
C
C NS IS THE NUMBER OF SHELLS TO BE SUMMED
C
NS=13
C
C READ INPUT DATA
C
READ(5,1) HOL
1 FORMAT(20A4)
READ(5,8) (AF(I),BF(I),I=1,4)
8 FORMAT(8F9.4)
READ(5,10) (AN(I),D(I),PHI(I),I=1,NS)
10 FORMAT(3Fb.0)
WRITE 6,2)HOL
2 FORMAT(1H1,20A4)
WRITE(6,11) (AN(I),PHI(I),I=1,NS)
11 FORMAT(1X,3F6.4)
N=499
C
C GENERATE ENERGY VALUES
C
DO 100 I=1,N
XI=I
E(I)=2.*XI
E1=E(I)
C
C DEFINE K USING EQ(2-16) AND(2-35)
C
K(I)=SQRT(.263*(E1+10))
K1=K(I)

```

C SS=K1*K1/(16*PI*PI)
C DOYLE AND TURNER SCATTERING FACTOR
C
F=AF(1)*EXP(-BF(1)*SS)+AF(2)*EXP(-BF(2)*SS)+AF(3)*EXP(-BF(3)*SS
1 +AF(4)*EXP(-BF(4)*SS)
C
C DEFINE LINEAR PHASE SHIFT
C
ETA(I)=-.245*K1+7.95
CHI=0.0
C
C SUM OVER COORDINATION SHELLS
C
DO 200 J=1,NS
R=A*D(J)
ARG=K1*A*D(J)
ARG2=ARG+ETA(I)
RHO(J)=-K1*AN(J)*SIN(2.*ARG2)/ARG**2
C
C SCATTERING CORRECTION
C
RHO(J)=RHO(J)*K1*F
C
C TEMPERATURE CORRECTION
C
RHO(J)=RHO(J)*EXP(-.0265*K1**2*PHI(J))
C
C RANGE TERM
C
RHO(J)=RHO(J)*EXP(-.3*D(J)*A)
CHI=CHI+RHO(J)
CHI2(I,J)=CHI
CMIN=A MIN1(CMIN,CHI2(I,J))
CMAX=A MAX1(CMAX,CHI2(IMJ))
C(1)=CMIN
C(2)=CMAX
200 CONTINUE
C
C WRITE OUTPUT DATA
C
30 WRITE (6,30) el,K1,CHI2(I,1),CHI2(I,3),CHI2(I,NS)
30 FORMAT(1X,F7.1,F8.4,3(2X,E12.4))
100 CONTINUE
C
C PLOTTING DATA FOR CALCOMP
C
INTEGER I BUF(1024)
WRITE(6,3)
3 FORMAT(11HOBEGIN PLOT)

```

```
CALL PLOTS(JBUF,1024,0)
CALL PLOT(0.,1.5,-3)
CALL SCALE(E,10.,N,1)
CALL SCALE(C,9.,2,1)
CALL AXIS(0.,0.,1HE,-1,10.,0.,E(N+L),E(N+2))
CALL AXIS(0.,0.,3HCHI,3,9.,90.,C93),C(4))
CALL SYMBOL(0.,-.8,.1,HOL,0.,80)
DO 40 J=NS,NS
  CHI2(N+1,J)=C(3)
  CHI2(N+2,J)=C(4)
  CALL LINE(E,CHI2(1,J),N,1,0,0)
40 CONTINUE
  CALL PLOT(12.,-1.5,999)
  WRITE(6,4)
4 FORMAT(9HOEND PLOT)
  STOP
  END
```

References

1. R.L. de Krönig, Z. Physik 70, 317 (1931); 75, 91 (1932).
2. L.G. Parratt, Rev. Mod. Phys. 31, 616 (1969).
3. L.V. Azaroff, Rev. Mod. Phys. 35, 1012 (1963).
4. T. Hayasi, Sci. Repts. Tohoku Univ. 33, 123; 183 (1949); 34, 185 (1950).
5. R.L. de Krönig, Z. Physik 76, 468 (1932)
6. H. Petersen, Z. Physik, 80, 253 (1933)
7. A.I. Kostarev, Zh. Eksperim. i Theor. Fiz., 11, 60 (1941); 19, 413 (1949); 20, 811 (1950).
8. A.T. Kozlenkov, Bull. Acad. Sci. USSR, Ser. Phys., 25, 968 (1961).
9. T. Shiraiwa, T. Ishimura and M. Sawada, J. Phys. Soc. Jap. 13:8, 848 (1958).
10. F.W. Lytle, "Advances in X-ray Analysis", Vol. 9, p. 398, Mallet, Fay, Mueller, ed. (Plenum, New York, 1966).
11. B. Roulet, J. Gavoret, and P. Nozieres, Phys. Rev. 178:3, 1012 (1969).
12. H. Bethe and E. Salpeter, "Quantum Mechanics of One and Two Electron Systems", Sec. 59 and 69 (Springer-Verlag, Berlin, 1957).
13. J.W. Cooper, Phys. Rev. 128:2, 681 (1962).
14. M. Lax, Rev. Mod. Phys. 23, 287 (1951).
15. E.A. Stern, Phys. Rev. 188:3, 1163 (1969).
16. L.S. Rodberg and R.M. Thaler, "Introduction to the Quantum Theory of Scattering", p. 34 (Academic Press, New York, 1967).
17. D.L. Mott, Ph.D. Thesis (unpublished), New Mexico State University (1963).
18. J.C. Slater, "Quantum Theory of Atomic Structure," Vol. 1, p. 206 (McGraw-Hill, New York, 1960).
19. P.A. Doyle, and P.S. Turner, Acta. Cryst. A24, 390 (1968).
20. Roy Kaplow, T.A. Rowe and B.L. Averbach, Phys. Rev. 168, 1068 (1968).

21. V.V. Shmidt, Bull. Acad. Sci. USSR, Ser. Phys., 25, 988 (1961).
22. V.V. Shmidt, Bull. Acad. Sci. USSR, Ser. Phys. 27, 392 (1963).
23. F.W. Lytle, Developments in Applied Spectroscopy, Vol. 2, p. 285 (Plenum, New York, 1963).
24. J.D. Hanawalt, Z. Physik 70, 293 (1930); J. Franklin Inst. 214, 569 (1932).
25. T. Boster and J. Edwards, Phys. Rev. 170:1, 12 (1968).
26. J.A. Jope, J. Phys. C. Ser. 2, Vol. 2, 1817 (1969).
27. F. Herman and S. Skilman, "Atomic Structure Calculations", (Prentice Hall, Englewood Cliffs, 1963).
28. B.E. Warren, X-ray Diffraction, p. 217 (Addison-Wesley, Reading, 1969).
29. R. Kaplow, S.L. Strong, B.L. Averbach, Phys. Rev. 138:5A, A1136 (1965).
30. N.J. Shevchik, Ph.D. Thesis (unpublished), Harvard University (1971).
31. M. Abramowitz and I.A. Stegun, "Handbook of Mathematical Functions", p. 299, National Bureau of Standards Applied Math Series #55 (1965).
32. J.A. Bearden, Rev. Mod. Phys. 39:1, 78 (1967).
33. R. Grigorovici and R. Manaila, Thin Solid Films, 1, 343 (1968).
34. R. Grigorovici and R. Manaila, J. Non-Cryst. Solids, 1, 371 (1969).
35. D.E. Polk, J. Non-Cryst. Solids, 5, 365 (1971).
36. W.H. Zachariasen, J. Am. Chem. Soc. 54, 3841 (1932).
37. S.C. Moss and J.F. Graczyk in Proc. 10th Intl. Conf. Phys. Semiconductors, AEC Conf. 700801, S.P. Keller, J.C. Hensel, F. Stern, ed., p. 658 (1970).
38. N.J. Shevchik and William Paul, J. Non-Cryst. Solids (to be published).
39. R.D. Heidenreich, "Fundamentals of Transmission Electron Microscopy", Chapter 1 (Interscience, New York, 1964).
40. H.S. Chen and D. Turnbull, J.A.P. 40, 4214 (1969).

41. H. Richter and G. Breiting, Z. Naturforschung, 13a, 988 (1958).
42. W.F. Nelson, I. Siegel and R.W. Wagner, Phys. Rev. 127, 6 (1962).
43. F.W. Lytle, "Physics of Non-Crystalline Solids", p. 12, J.A. Prins, ed. (North Holland, Amsterdam, 1964).
44. R.W.G. Wyckoff, Crystal Structures, 2nd ed., Vol. 1, p. 312 (Interscience, New York, 1963).
45. J. Zarzycki, Verres Re'fract. 11, 3 (1957).
46. E.H. Henninger, R.C. Buschert, and L. Heaten, J. Phys. Chem. Solids 28, 423 (1967).
47. R.L. Mozzi, and B.E. Warren, J. Appl. Cryst. 2, 164 (1969).
48. D.L. Evans and S.V. King, Nature 212, 1353 (1966).
49. Ref. 44, p. 316.
50. Ref. 44, p. 102.
51. A.F. Wells, Structural Inorganic Chemistry", p. 527, (Oxford, London, 1962).
52. Ch'Unhua, et al, Russ. J. Inorg. Chem., 7, 496 (1962); 7, 1117 (1962).
53. A.I. Kostarev and W.M. Weber, Phys. Rev. B 3, 4124 (1971).
54. N.F. Mott, Advances in Physics 16, 49 (1967).
55. M.H. Cohen, H. Fritzsché, S.R. Ovshinsky, Phys. Rev. Lett., 22, 1065 (1969).
56. J.W. Cooley and J.W. Tukey, Mathematics of Computation 19, 297 (1965).